國立臺灣大學電機資訊學院電機工程學系

博士論文

Department of Electrical Engineering
College of Electrical Engineering and Computer Science
National Taiwan University
Doctoral Thesis

超音波小動物影像之元件與方法
Devices and methods for ultrasonic small animal imaging

劉建宏

Jian-Hung Liu

指導教授：李百祺 博士

Advisor: Pai-Chi Li, Ph.D.

中華民國 97 年 7 月

July, 2008

國立臺灣大學電機工程學研究所
博士學位論文

超音波小動物影像之元件與方法

研 究 生：劉建宏

指導教授：李百祺 教授

經考試合格特此證明

博士學位論文考試委員：

吳政忠

李百祺

葉秩光

指導教授 ：李百祺

研究所所長：胡振國

中華民國九十七年 七月

中文摘要

小動物模型在臨床前研究已被廣泛使用，發展先進之小動物影像技術亦因此成為一重要工作。本論文之目標，即為針對小動物超音波影像所面臨之限制，提出解決之道，並進一步提升超音波於小動物影像之功能。本論文分為三主要項目，第一部分為針對小鼠心臟影像掃描速率不足之問題，以心電圖觸發技術克服，使得以機械掃描為主之超音波小鼠影像，在不需要使用高速馬達或輕量探頭之條件下，亦能以區塊掃描或單線掃瞄之方式，完整的捕捉小鼠心臟之運動細節。本研究之第二部分，則為提出並實現一提升高頻超音波探頭頻寬之技術。本技術之關鍵，在於成功的開發出高頻探頭製程，製作出單一陣元、環型、但具有非均勻厚度之高頻探頭，使得頻寬可達到 20-30%之提升，靈敏度則下降 3.1dB。使用此類探頭，不僅解析度得以提升，亦使得非線性影像等需要較高頻寬之先進影像技術，得以更有效之實現。本論文之第三部分，則為將寬頻探頭技術應用至小動物光聲影像，以更有效的進行超音波與光聲之多模式影像。使用此技術，不僅超音波與光聲影像可以各自工作在其最適合之頻率範圍內，以提供最適合之解析度與林靈敏度，本技術亦可以用來提升光聲影像之對比度，更成功的鑑別出不同光吸收係數之區域。本論文成功的開發多種適用於小動物影像之方式與元件，有效的提升影像的時間、空間、對比解析度，將有助於小動物影像之分析。論文最後亦將探討相關技術可能之延伸應用。

關鍵詞：高頻超音波影像、小動物影像、光聲影像、心電圖觸發影像、寬頻高頻探頭、雙頻光聲探頭

Abstract

Small animal models have been widely used in preclinical research, and therefore developing advanced small imaging technologies has also become an important task. The goal of this study is to propose solutions that can overcome and current limitations of small animal ultrasonic imaging and further improve its imaging performance. To this end, this thesis consists of three major components. The first part is to overcome the frame rate limitation of small animal cardiac imaging. The limitation is due to the fact that the mechanical scanning of small animal ultrasonic imaging is not sufficiently fast to capture the motion details of a mouse heart. By using mouse ECG to trigger the imaging system, a block scanning method and a line scanning method were developed that can effectively achieve an imaging frame rate in the kHz range. In addition, this method can be implemented without the need of an ultrafast motor or a light-weight transducer. The second part of this thesis describes design and implementation of a high frequency ultrasound transducer with enhanced bandwidth. The transducer is a single element annular transducer, and the thickness of the piezoelectric material varies from ring to ring. By doing this, each ring has a distinct frequency response and thus the bandwidth is enhanced when all the rings are excited at the same. With this, the bandwidth can be improved by 20-30%, at the price of 3.1dB reduction in two-way insertion loss. Such a transducer can also be used to improve axial resolution as well as harmonic imaging. In the third part of this thesis, the multi-band transducer technology that we developed previously was extended to ultrasonic/photoacoustic multi-modality small animal imaging. By using multiple bands, we can ensure that both imaging modalities can be operated in the optimal frequency range, so that good spatial resolution and sensitivity can be achieved at the same time. In addition, the transducer can also be used to improve the contrast in photoacoustic imaging, because objects with different optical absorption generate ultrasound in different frequency ranges. In summary, advanced devices and imaging methods were developed in this study for preclinical small animal research. These methods can be used to improve temporal, spatial and contrast resolution, and thus to assist small animal research. Potential extended applications of these devices and methods will also be discussed.

Keywords: high frequency ultrasound, small animal imaging, photoacoustic imaging, ECG triggered imaging, wideband high frequency transducer, two-band photoacoustic transducer.

Contents

List of Figures

List of Tables

Chapter 1. Introduction

1.1 small animal in biomedical research

Small animal models are widely applied in genomics research, drug development and disease research [1-3]. For example, murine genotype can be manipulated, providing opportunities to investigate effects of similar manipulations on human. Moreover, mice have short life spans so they can be studied throughout their entire life and even through several generations within a short period of time. The murine models are also a helpful tool to recapitulate aspects of human physiology [4].

A non-invasive, small animal imaging system with high spatial resolution and high sensitivity is beneficial to the murine model preclinical research. With such a system, the need to sacrifice animals can also be reduced. Nonetheless, because of the small size, it is challenging to provide sufficient resolution to meet the needs of small animal imaging [5, 6]. The commonly adopted small animal imaging modalities are listed in Table 1.1. Among them, ultrasonic imaging has several advantages [4-6]. On one hand, it is safe because of non-ionizing radiation. On the other hand, it is real-time and can be used to image a wide variety of internal organs with sufficient penetration and resolution.

Table 1.1 Features of the most common imaging techniques [5]

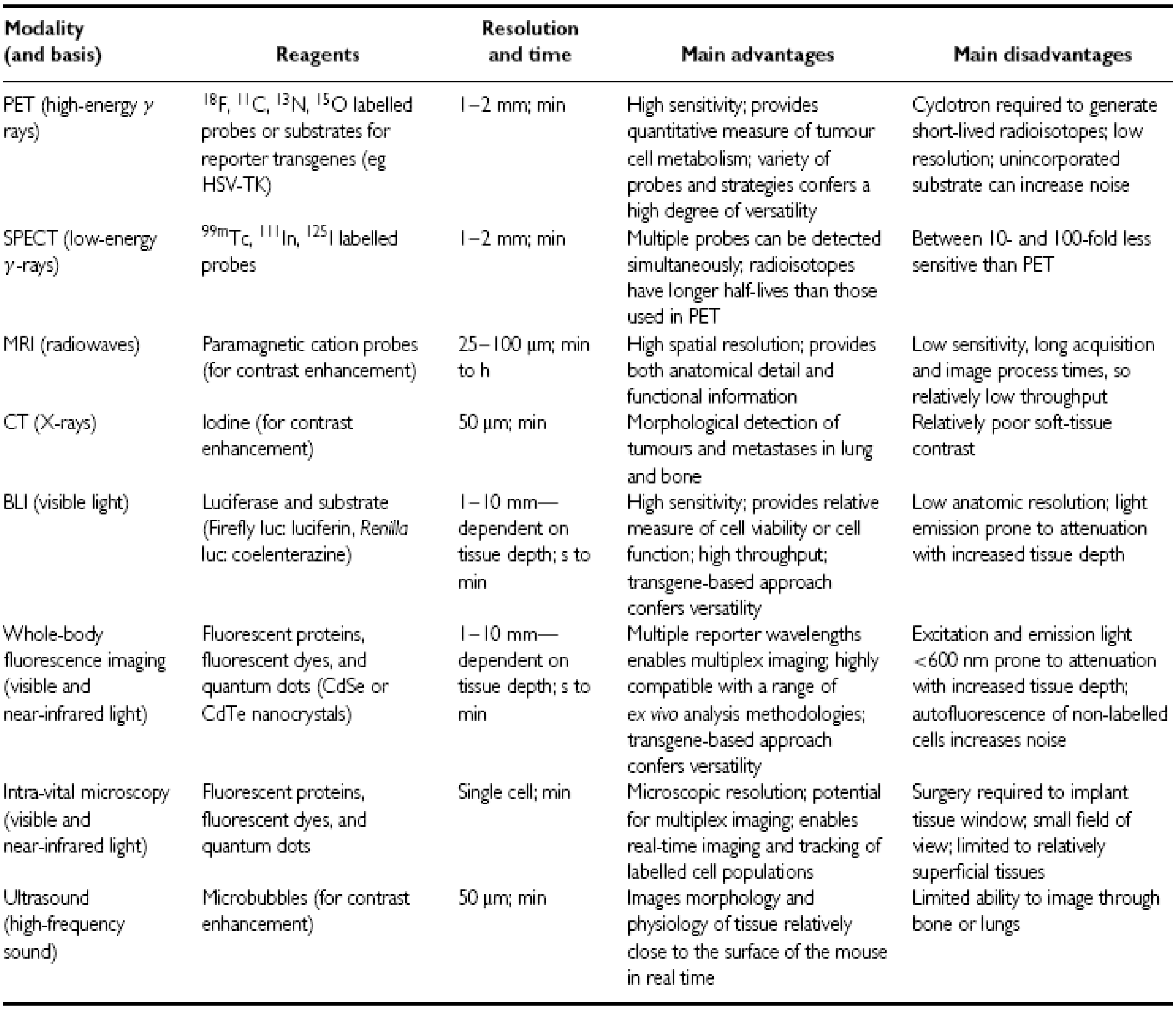

Modality (and basis)	Reagents	Resolution and time	Main advantages	Main disadvantages
PET (high-energy γ rays)	^{18}F, ^{11}C, ^{13}N, ^{15}O labelled probes or substrates for reporter transgenes (eg HSV-TK)	1–2 mm; min	High sensitivity; provides quantitative measure of tumour cell metabolism; variety of probes and strategies confers a high degree of versatility	Cyclotron required to generate short-lived radioisotopes; low resolution; unincorporated substrate can increase noise
SPECT (low-energy γ-rays)	^{99m}Tc, ^{111}In, ^{125}I labelled probes	1–2 mm; min	Multiple probes can be detected simultaneously; radioisotopes have longer half-lives than those used in PET	Between 10- and 100-fold less sensitive than PET
MRI (radiowaves)	Paramagnetic cation probes (for contrast enhancement)	25–100 μm; min to h	High spatial resolution; provides both anatomical detail and functional information	Low sensitivity, long acquisition and image process times, so relatively low throughput
CT (X-rays)	Iodine (for contrast enhancement)	50 μm; min	Morphological detection of tumours and metastases in lung and bone	Relatively poor soft-tissue contrast
BLI (visible light)	Luciferase and substrate (Firefly luc: luciferin, *Renilla* luc: coelenterazine)	1–10 mm—dependent on tissue depth; s to min	High sensitivity; provides relative measure of cell viability or cell function; high throughput; transgene-based approach confers versatility	Low anatomic resolution; light emission prone to attenuation with increased tissue depth
Whole-body fluorescence imaging (visible and near-infrared light)	Fluorescent proteins, fluorescent dyes, and quantum dots (CdSe or CdTe nanocrystals)	1–10 mm—dependent on tissue depth; s to min	Multiple reporter wavelengths enables multiplex imaging; highly compatible with a range of *ex vivo* analysis methodologies; transgene-based approach confers versatility	Excitation and emission light <600 nm prone to attenuation with increased tissue depth; autofluorescence of non-labelled cells increases noise
Intra-vital microscopy (visible and near-infrared light)	Fluorescent proteins, fluorescent dyes, and quantum dots	Single cell; min	Microscopic resolution; potential for multiplex imaging; enables real-time imaging and tracking of labelled cell populations	Surgery required to implant tissue window; small field of view; limited to relatively superficial tissues
Ultrasound (high-frequency sound)	Microbubbles (for contrast enhancement)	50 μm; min	Images morphology and physiology of tissue relatively close to the surface of the mouse in real time	Limited ability to image through bone or lungs

1.2 Basics of imaging resolution

Resolution is an important factor for ultrasound imaging. There are spatial, contrast and temporal resolutions that must be considered in imaging. Temporal resolution is determined by the number of image frames acquired per unit time (i.e., frame rate). It is particularly important when there are structures which that move rapidly inside the human body. In order to obtain a clear image of these structures and assess motion details, the time needed to acquire an image should be sufficiently short. The frame rate of the ultrasonic system is determined by the number of scan lines in an image and the pulse repetition frequency (PRF), which is determined by penetration depth. Therefore, there is a tradeoff between PRF and the image depth.

In high frequency ultrasound, because mechanical scanning (instead of electronic scanning) is used, the frame rate is often limited. This is a particularly severe limitation when imaging fast moving objects such as the mouse heart. Therefore, the first major goal is to develop a method that can effectively increase the image frame rate by using the existing mechanical scanning setup.

For single element transducers, geometric focusing is typically done to achieve good beam quality. The pressure field from a circular transducer can be represented using the impulse response theory [7]. At a particular point in the field, the pressure can be described as:

$$p(\vec{r},t) = -\rho \frac{\partial V_0(t)}{\partial t} * h(\vec{r},t) \qquad (1.1)$$

where $\vec{r}$ represents the observation point, V_0 is the velocity at the transducer surface, and h is the impulse response of the aperture. Simplified expressions for lateral resolution, axial resolution, and depth of field (DOF) for a spherical source at the focus are described in the following equations.

$$\text{Lateral resolution} = \text{F-number} \cdot \lambda \qquad (1.2)$$

$$\text{axial resolution} \cong c \cdot \Delta t/2 \qquad (1.3)$$

$$\text{DOF} = 7\lambda(\text{F-number})^2 \qquad (1.4)$$

where c is the sound velocity, λ is the wavelength, Δt is the pulse duration. The axial and lateral resolutions can be improved when frequency is increased. A higher operating frequency, which corresponds to a smaller wavelength, provides better resolution. This is the main reason why higher acoustic frequencies have been used in small animal imaging.

Spatial resolution is further divided into axial, elevational and lateral resolutions. Lateral resolution is defined as the minimum separation of two distinct structures projected along the direction perpendicular to the ultrasound beam. Fig. 1.1 shows the beam pattern of a single element transducer. The transducer provides the best resolution near the geometrically focused location, but the performance out of the focus deteriorated noticeably. The elevational resolution is also similarly defined, except that the direction perpendicular to the image plane is of interest.

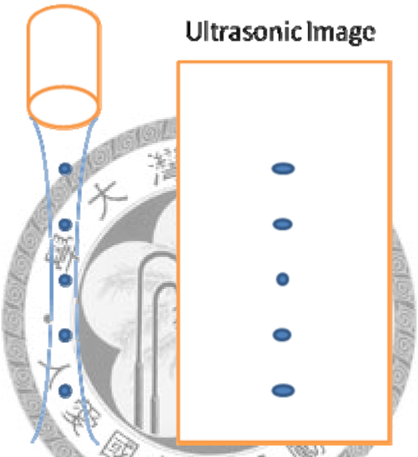

Fig. 1.1 Illustration of lateral resolution

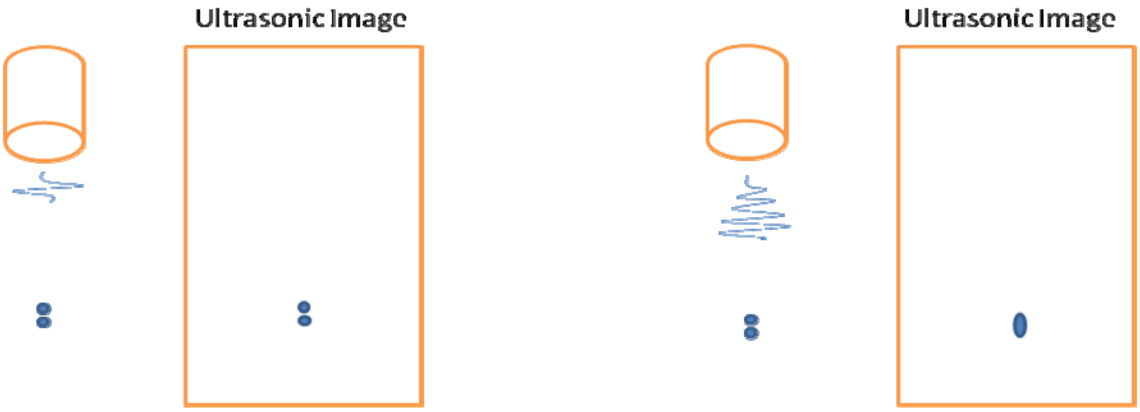

Fig. 1.2 Illustration of axial resolution

The axial resolution is the minimum distance in the beam direction between two reflectors which can be identified as separate objects. The length of the ultrasound pulse is a main factor to determine the axial resolution. Two objects resolvable if the pulse duration is shorter than the distance between the structures. Fig. 1.2 shows the relation between the pulse duration and the axial resolution. If the pulse length is longer than the distance between the objects, only a single reflection can be detected and only one object is shown in the image. To achieve good axial resolution, a wide bandwidth is desired. It is the second main goal of this study to design and fabricate a high frequency transducer that can provide a wider bandwidth, and thus improved axial resolution can be expected.

Contrast resolution refers to the ability to differentiate objects of certain areas with different mean brightness values. It is often more important than spatial resolution in most imaging situations. Intuitively, an imaging system's ability to detect objects of low contrast against the background is determined by the following three factors: contrast, size of the object and noise level. In ultrasonic imaging where speckle noise is present, contrast resolution can also be improved by improving spatial resolution. In this thesis, not only the contrast resolution in ultrasonic imaging can be improved by using a wideband transducer, we will further develop a new method that can be used to improve contrast resolution in photoacoustic imaging using the same transducer technology. .

1.3 Organization of the thesis

The primary objective of this thesis is to develop device and imaging technologies to improve imaging performance in small animal studies. As previously mentioned, the efforts toward this goal are organized in three main components. The first one is to develop two scanning methods to improve temporal resolution for imaging of the mouse heart. The second part is the design, fabrication, and evaluation of a single element annular transducer, which is based on non-uniform thickness of concentric elements of the same piezoelectric material. It increases the bandwidth and depth of field as compared with the conventional ultrasound transducer. The third part of this thesis is using the same transducer technology to develop a dual band photoacoustic transducer. The detector effectively received photoacoustic and ultrasonic signals by using proper frequency bands. The contrast of photoacoustic image can be improved by properly selecting signal bandwidth of the receiver.

Chapter 2 presents a high frequency ultrasonic imaging system for murine cardiac imaging. Two scanning methods have been developed. One is based on electrocardiography (ECG) triggering and is called the block scanning mode, in which the murine cardiac images from the end-systolic and end-diastolic phases are retrospectively reconstructed within a relatively short data acquisition time using the ECG R-wave as the trigger to the imaging system. The other method is the line scanning mode based on ECG gating, in which both ECG and ultrasound scan lines are continuously acquired over a longer time, enabling images during the entire cardiac cycle to be obtained. It is demonstrated here that the effective frame rate is determined by the pulse repetition frequency, and can be up to 2 kHz in the presented system.

Chapter 3 describes components of a single element ultrasound transducer. Performance of transducers operating at high frequencies is greatly influenced by properties of the piezoelectric materials. In particular, selection of an appropriate material for a transducer is based upon many factors, including piezoelectric constant, dielectric constant, sound velocity, and acoustic impedance. Appropriate selection of the materials can improve sensitivity and bandwidth of ultrasound transducer.

Chapter 4 discusses design, fabrication, and evaluation of a high-frequency single-element transducer. The transducer has an annular geometry, with the thickness of the piezoelectric material increasing from the center to outside. This single-element annular transducer (SEAT) can provide a broader frequency range than a conventional single-element transducer with a uniform thickness (single-element uniform transducer, SEUT). We compared the characteristics of a SEUT and a SEUT: both transducers used 36°-rotated, Y-cut lithium niobate (LiNbO3) material. Overall the bandwidth of the SEAT was 20-30% larger than that of the SEUT. However, the two-way insertion loss of the SEAT was 19.5 dB, while 16.4 dB for the SEUT. The acoustic beam pattern of the SEAT was also evaluated numerically by finite-element simulations and experimentally by an ultrasound beam analyzer. The SEAT can be used for imaging applications that require a wide transducer bandwidth, such as harmonic imaging, and can be manufactured using the same techniques used to produce transducers with multiple frequency bands.

Chapter 5 discusses fabrication and performance of a dual frequency photoacoustic transducer (DFPT). The DFPT has a diameter of 6 mm and comprises two concentric rings of equal area whose center frequency of the outer and inner elements are 4.9 MHz and 14.8 MHz, respectively. Acoustic matching layers of DFPT were made to uniform thickness, which respectively corresponded to 3/4 and 1/4 wavelength for inside and outside elements. There is a 0.65 mm hole in the DFPT surface for insertion of optical fiber that can solved conventional device-situating problem. Phantom results indicate that the DFPT can further enhance the contrast in photoacoustic imaging. Its potential for contrast improvement of objects with a significantly higher absorption is revealed.

Finally, conclusions, discussion, and future works are described in chapters 6 and 7.

Chapter 2. ECG Triggering and Gating for Ultrasonic Small Animal Imaging

2.1 Introduction

Cardiovascular diseases are the leading cause of death in developed countries. It is usually characterized by blocked arteries, affecting the heart, brain and other vital organs. These lead to disability and death for hundreds of thousands of the world each year [11,12]. The murine models are usually used to study the development and progression of the human disease. Early studies of heart diseases are often performed in mice because the mouse cardiac system is very similar to that of human. Thus, understanding the structure and function of the mouse heart enables us to better understand the human heart [13-18]. Additionally, transgenic methods have been successfully applied to developing murine models for altering cardiac size and function. Therefore, tracking anatomical and physiological changes of the mouse heart is of great clinical significance. Although these tasks can be performed by necropsy or by various catheterization techniques, such techniques are invasive and hence difficult to replicate on the same animal. Moreover, they do not provide sufficient details on the chamber anatomy and dimensions.

Echocardiography refers to ultrasound imaging of the heart. It can provide much powerful information of the heart, including the size and shape, the pumping capacity and the location and extent of any damage of myocardium. It is a good way to detect these problems in their early stages before they become too serious. The clinical echocardiography systems (1-10 MHz) can provide useful information in humans, but their spatial resolution is not sufficient for small animals. The spatial resolution of clinical scanners is in the order of millimeters for transthoracic echocardiography, whereas the entire size of the animal organs is less than this scale. The spatial resolution becomes even more important when imaging small targets such as murine organs. For example, the left ventricular (LV) chamber diameter of a mouse heart is 2 to 3 mm and the LV posterior wall is approximately 0.6 mm thick at end diastole [19]. In order to obtain sufficient spatial resolution, the ultrasound center frequency needs to be higher than 20 MHz, which corresponds to a wavelength of less than 100 μm, yet a higher center frequency reduces tissue penetration. There is a tradeoff between frequency and penetration. According to the paper proposed by F. S. Foster et al [20], a the depth of a 5 MHz ultrasound transducer ranges from 12 to 15 cm, but the depth of a 10 MHz ultrasound transducer may image to a depth of only ranges from 3 to 4 cm. If the frequency becomes higher, the depth could only reach to a depth about 1 or 2 cm. Hence, increasing axial and lateral resolution by increasing frequency limits the penetration depth. However, the constraints do not influence the imaging on mice because the depths of most of the target organs are within 0.5 cm to 2 cm under the skin. If the entire mouse heart needs to be observed, the imaging frequency is limited to a range between 20-50 MHz.

The temporal resolution is a critical factor when target organs are rapid moving. The heart beat rates is higher than 300 beats per minute (bpm) for small animals ($\leq$ 50g). Due to fabrication difficulties, high frequency transducers are made in the form of single element where the imaging frame rate is limited to mechanical scanning. Therefore, mouse echocardiography has been restrained by the technical challenges to assess cardiac functions at such a rapid heart rate. For example, a heart rate of small animal is about 300 bpm, an acquisition frame rate of 30 Hz would only capture six images in a cardiac cycle. Moreover, each image frame demonstrates 17% of the cardiac cycle. It makes the accurate determination of absolute end-diastolic and end-systolic volume difficult. Although an ultrasound system with higher center frequency offers better spatial resolution, the system have low imaging frame rate for the cardiac structure. The low temporal resolution is not sufficient to image the rapid movement of a mouse heart. Furthermore, the resultant images will suffer from data misalignment.

Image alignment is more complicated for the heart than for other organs due to the rapid and flexible motion of the myocardium, and is a critical problem in several imaging modalities [21]. In general, electrocardiography (ECG) is employed to minimize imaging artifacts caused by cardiac motion [22]. For example, perspective ECG triggering and retrospective ECG gating have been used in computed tomography [23]. Prospective ECG triggering uses ECG signals in computed tomography such that X-rays are generated and projection data are acquired synchronously. In contrast, in retrospective ECG gating the projection data and ECG signals are acquired simultaneously, and the images corresponding to different phases in a cardiac cycle are subsequently reconstructed by selecting appropriate temporal windows of the acquired projection data.

This chapter applies ECG triggering and gating to ultrasonic small animal imaging to develop block and line scanning modes, respectively. With these techniques, images acquired during multiple cardiac cycles are used to reconstruct complete images, which resolves the misalignment problem and results in a significant increase in the frame rate. The proposed system is fine spatial resolution which is achievable even at very high frame rate. The frame rate is high enough to observe different cardiac phases of small animals. The effective temporal resolution is only limited by the pulse repetition frequency of the imaging system. Here the methods are described in details, and demonstrated using both phantom data and *in vivo* mouse data.

2.2 High frequency ultrasonic animal imaging system

Our high frequency ultrasonic imaging system consists of a high frequency single-element focused transducer (NIH Resource Center for Medical Ultrasonic Transducer Technology, Penn State University Park, PA), a 200-MHz arbitrary waveform generator (AWG-420, Tektronix, Tokyo, Japan), a linear amplifier (25A250A, Amplifier Research, Souderton, PA), an ultrasonic receiver (5900PR, Panametrics, Waltham, MA), a micro stepping motor (MSAW016Y21, Sankyo, Tokyo, Japan), and a 500-MHz, 8-bit analog-to-digital (A/D) conversion card (PAD 500, Signatec, Corona, CA) [24]. The $LiNbO_3$ transducer has a center frequency of 45 MHz with a 55% –6dB fractional bandwidth, a diameter of 6 mm, and a geometric focus at 12 mm. Image scanning is performed mechanically with the micro stepping motor in a rectangular image format. Image reconstruction is performed and displayed on a personal computer using MATLAB (MathWorks, Natick, Waltham MA).

A micro stepping motor obtained from a DVD-ROM drive of a personal computer was modified for positioning the high frequency transducer. The control software was written in C++ with an advanced SCSI programming interface. The stepping accuracy was 1 μm and the maximum scanning speed was 100 mm/s.

2.2.1 The properties of biosignal recorder

Respiration and ECG signals of the mouse were recorded using a mouse board (Biosensor Technology Corporation, Taipei, R.O.C.,), which is a custom designed physiology monitoring recorder for small animals. The cardiac signal was measured from different electrodes and then amplified 5700-fold. The various phases of respiration are determined based on the measured impedance. In order to avoid interference between the cardiac and respiration signals, the two signals were individually passed through bandpass filters with pass bands of 8.5–35 Hz and 0.1–6.5 Hz, respectively. Typical ECG and respiration signals of the mouse are shown in Fig 2.1. R waves were detected using LabVIEW (National Instruments, Austin, TX) by determining when the slope changed from negative to positive, and the magnitude of the ECG signal was larger than the P wave and smaller than the potential spike signal produced by shivering. Positive and negative slopes of the respiration signal indicate inhalation and exhalation, respectively.

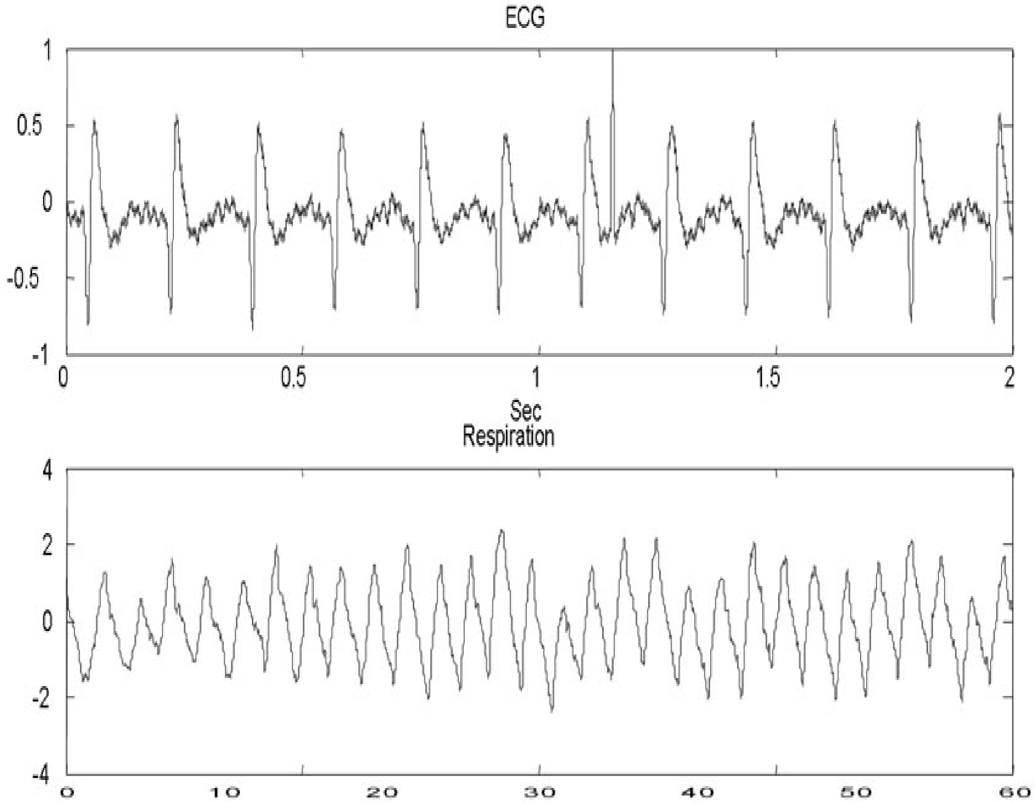

Fig. 2.1 ECG and respiration signals of mice

2.2.2 The coded excitation techniques

The high frequency transducer drives by pulse signal that cannot effective obtain penetration. Coded excitation techniques can be employed to improve the spatial resolution whilst maintaining the penetration. A chirp (i.e., linear FM) transmit waveform was used to improve the penetration depth [25]. To restore the axial resolution, a quadratic programming method was used to design the pulse compression filter. The chirp signal used in this study obeyed the following equation [26, 27]:

$$c(t) = g(t - \frac{T}{2})\cos\left[2\pi(f_1 t + \frac{f_2 - f_1}{2T}t^2)\right] \qquad (2.1)$$

where $g(t)$ is a Gaussian envelope function, T is the signal duration, and f_2 and f_1 represent the upper and lower operating frequencies, respectively. In all experiments of this study the following parameters were used: T = 4 μs, f_2 = 31.25 MHz, and f_1 = 18.75 MHz. Fig. 2.2 shows the designed chirp signal. The pulse-echo system response has to be known before the pulse compression filter can be designed. For this purpose, the echo from a metal plate placed in a water tank was measured, and is shown in Fig. 2.3. The measured pulse-echo signal was defined as $h(n)$, $n = 0$ to $N - 1$, where N is the number of samples. The compressed signal $r(n)$ after applying the compression filter $p(n)$, $n = 0$ to $M - 1$ (M is the length of the filter), becomes

$$r(n) = h(n) * p(n) \qquad (2.2)$$

where '$*$' denotes the convolution operation and $r(n)$ has $N + M - 1$ samples. Denoting k as the index where $r(n)$ has its peak value and S_s as the index set specifying the sidelobe region of $r(n)$, the optimal filter is found by

$$p_{\mathrm{opt}}(n) = \min \sum_{n=0}^{M-1} \left\| p(n) \right\|^2 \tag{2.3}$$

subject to

$$\begin{aligned} & r(k) = 1 \\ & \left| r(n) \right| \leq L, n \in S_{\mathrm{s}} \end{aligned} \tag{2.4}$$

where L denotes the peak sidelobe level. The purpose of Eq. (2.3) is to avoid amplifying the noise so as to improve the signal-to-noise ratio of the compressed output. In this study, L was –60 dB, the mainlobe corresponded to compression to a fractional bandwidth of 20%, and the filter length was 1.5 times the designed transmit waveform. Fig. 2.4 shows the envelope of the compressed signal.

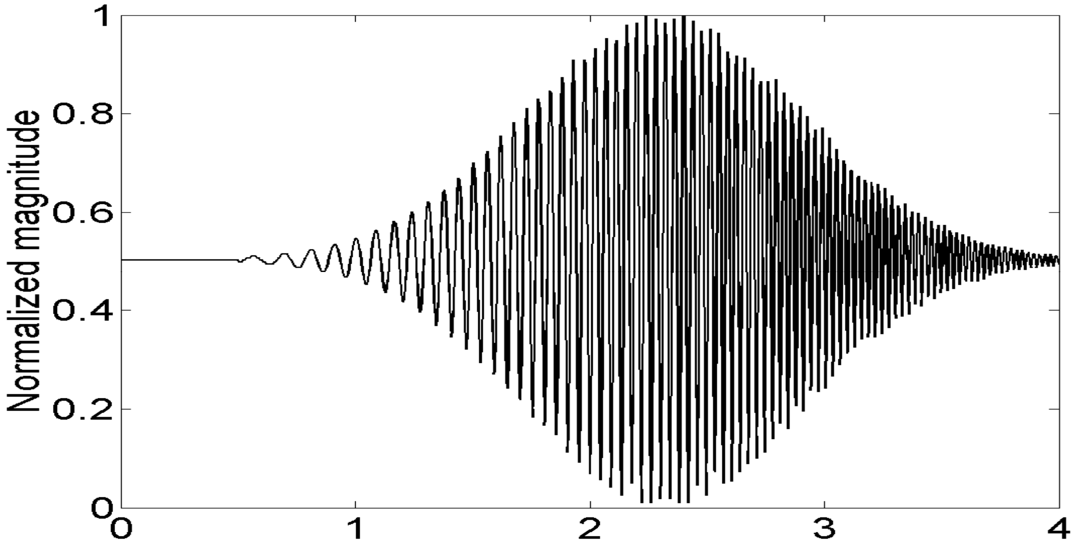

Fig. 2.2 Transmitted chirp signal. plate.

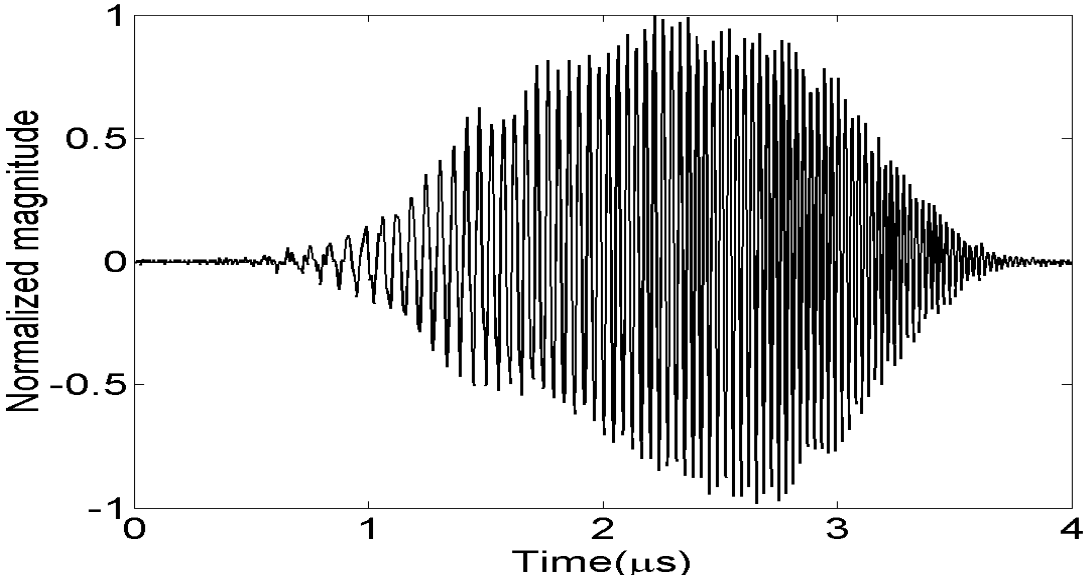

Fig. 2.3 Measured pulse-echo response from a metal

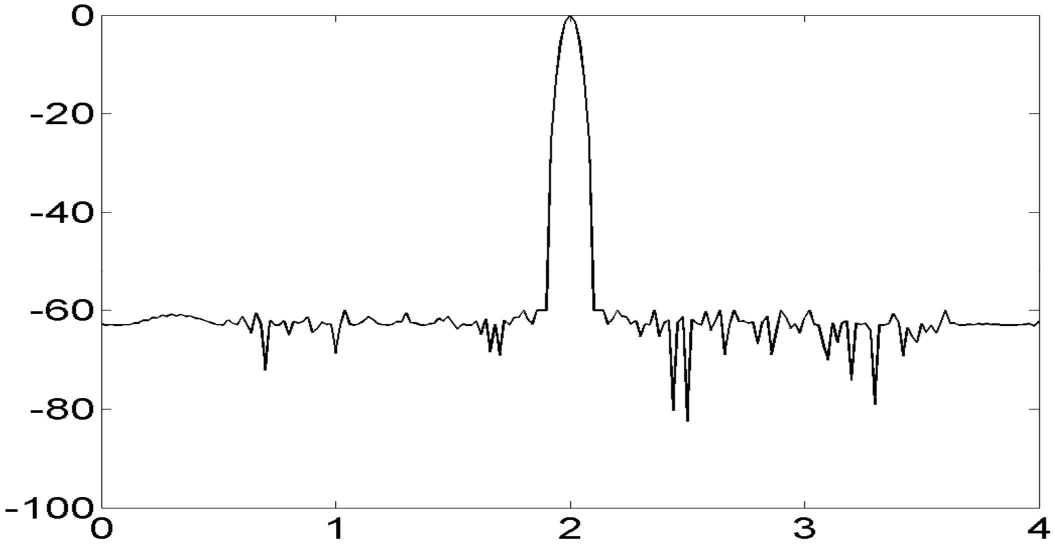

Fig. 2.4 Amplitude of the compressed signal.

2.3 Block and line scanning

A complete cardiac cycle is shown in Fig. 2.5 The myocardium motion is most stable in the end-systolic and end-diastolic phases, during which a group of scan lines can be acquired for retrospective image reconstruction. This is also referred to as the block scanning mode. Table 2.1 lists the durations of different cardiac phases [28]. The heart rate of mice is about 360 bpm, and the end-systolic and end-diastolic periods last for 10 ms and 16 ms, respectively. A schematic of the block scanning mode is shown in F2.6.

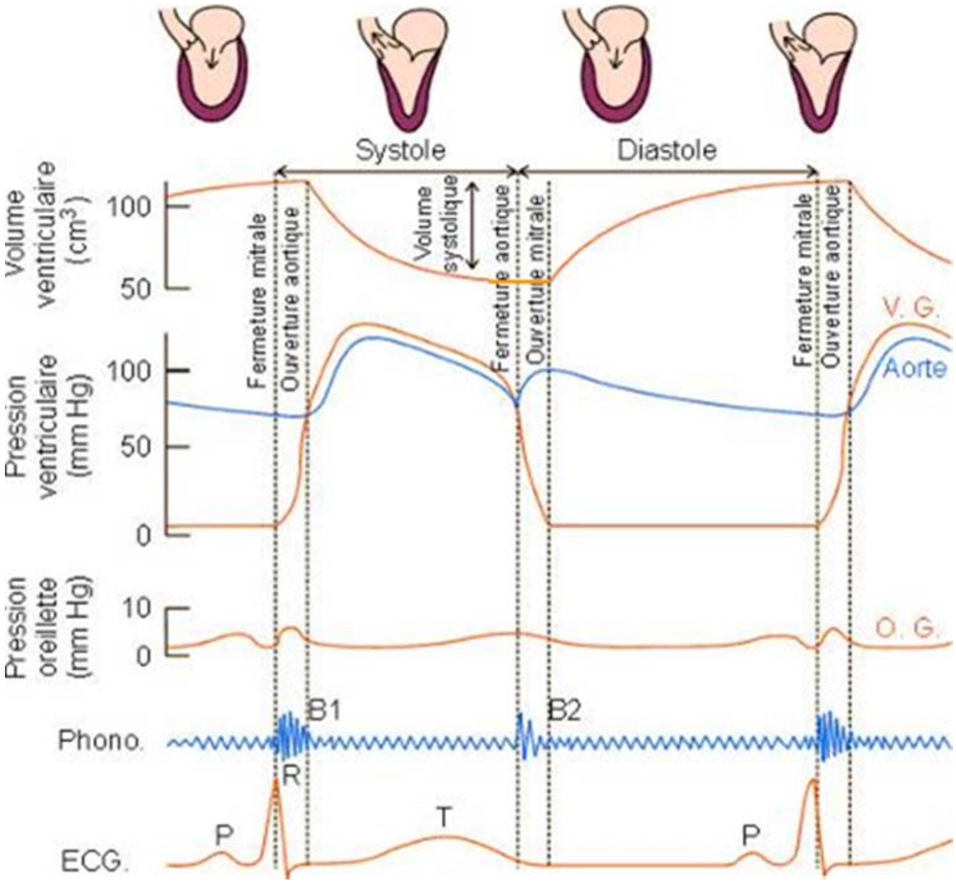

Fig. 2.5 The different heart phase in a cardiac cycle

The stepping motor moves the transducer continuously (i.e., the echoes are received while the transducer is moved), and the stepping motor, arbitrary waveform generator, and receiver are synchronized by the R-wave trigger. For the end-systolic images, the transducer movement and pulse-echo data acquisition occur after the R-wave trigger and last for 10 ms in each heartbeat. Heart images in this cardiac phase are then reconstructed using the data from different heartbeats and different scanning positions. Typically 10 mm of lateral scanning is required to cover a mouse heart, and this requires approximately 10 heartbeats to reconstruct an end-systolic cardiac image. Because the end-diastolic phase begins 54 ms after the R wave, as soon as the R wave has been present for 54 ms, the trigger signal is sent to the system to acquire the end-diastolic image data. The end-diastolic phase lasts for 16 ms, so that a 10-mm cardiac image is reconstructed during only seven consecutive heartbeats.

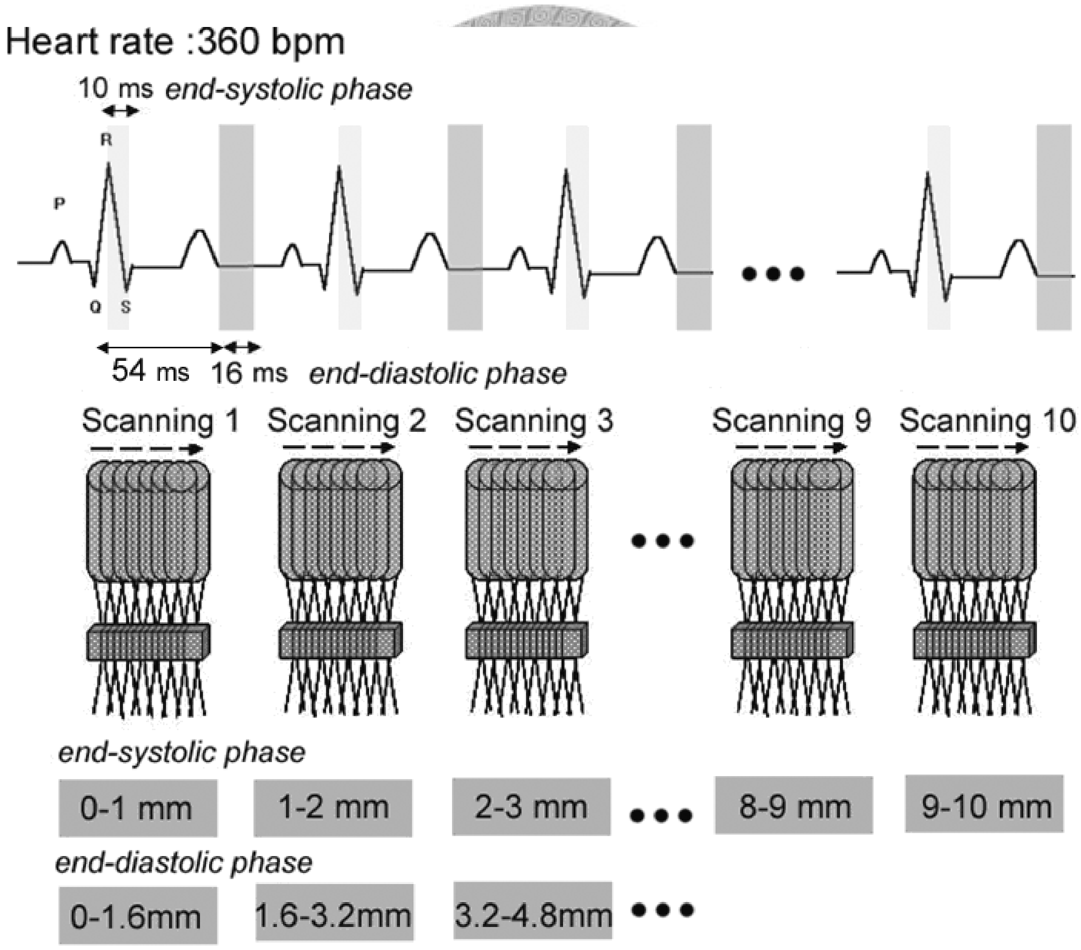

Fig. 2.6 Schematic of block scanning

Table 2.1 Durations of different cardiac phases

	Human	Mouse
Heart rate	72 bpm	360 bpm
Reduced filling	190 ms	38 ms
Atrial contraction	110 ms	22 ms
Isovolumetric contraction (end-systolic phase)	50 ms	10 ms
Rapid ejection	90 ms	18 ms
Reduced ejection	130 ms	26 ms
Isovolumetric relaxation (end-diastolic phase)	80 ms	16 ms
Rapid filling	110 ms	22 ms

A schematic of the line scanning mode is shown in Fig. 2.7 Unlike the block scanning mode in which swept scanning is performed, the line scanning mode uses step scanning, in which the echo signals are acquired at the same position in one entire R-R interval, then the transducer is moved to the next stepping position and waits for the onset of a new heartbeat. The total scanning time of this mode is equal to the number of scanning steps multiplied by the R-R interval. Images during the entire cardiac cycle can be reconstructed retrospectively. The effective frame rate of the reconstructed cardiac images is determined by the pulse repetition frequency of the transmitter, which was 2 kHz in our experiments. Typically 400 heartbeats are required to reconstruct a complete image sequence during an entire cardiac cycle.

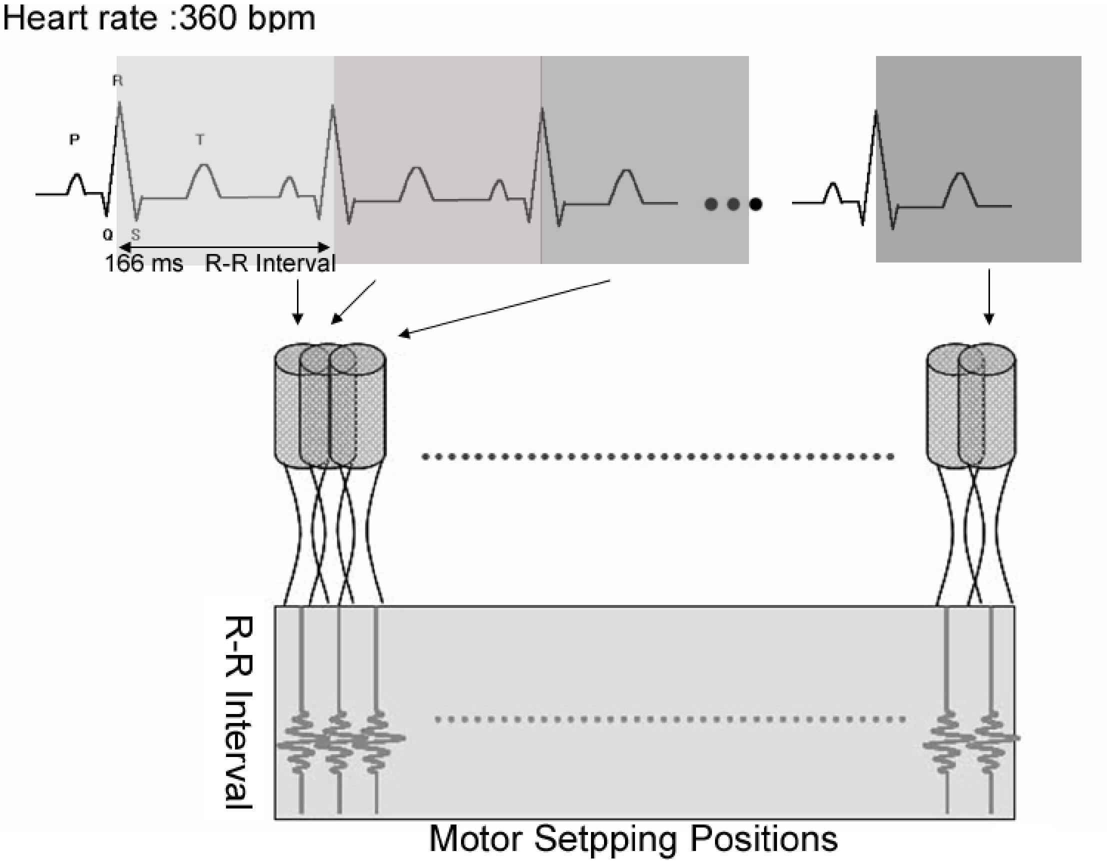

Fig. 2.7 Schematic of line scanning

2.4 Phantom experiments

A block diagram of the phantom experimental setup is shown in Fig. 2.8 The CompuFlow 1000 flow system (Shelley Medical Imaging Technologies, Ontario, Canada) is a computer controlled physiological flow simulator that pumps blood-mimicking fluid (Shelley Medical Imaging Technologies) according to a prestored pulsatile flow profile simulating normal mouse heart motion. A balloon is used to emulate the cardiac wall motion. The cardiac cycle of the CompuFlow 1000 flow system is 0.166 s. Holes on opposite sides of the balloon connect to the input and output tubes of the CompuFlow 1000 system, with fluid flowing through the balloon in a closed loop. The balloon is placed in a water tank, and its shape changes between contraction and relaxation when the blood-mimicking fluid passes through the flow system. An ECG output is also available from the CompuFlow 1000 system. R waves of the simulated ECG are detected using LabVIEW and used as the trigger. After the R-wave trigger, the arbitrary waveform generator sends out a chirp signal to drive the transducer and the A/D card starts to sample the echo signal at the same time. The proposed techniques were first investigated by evaluating images of the balloon.

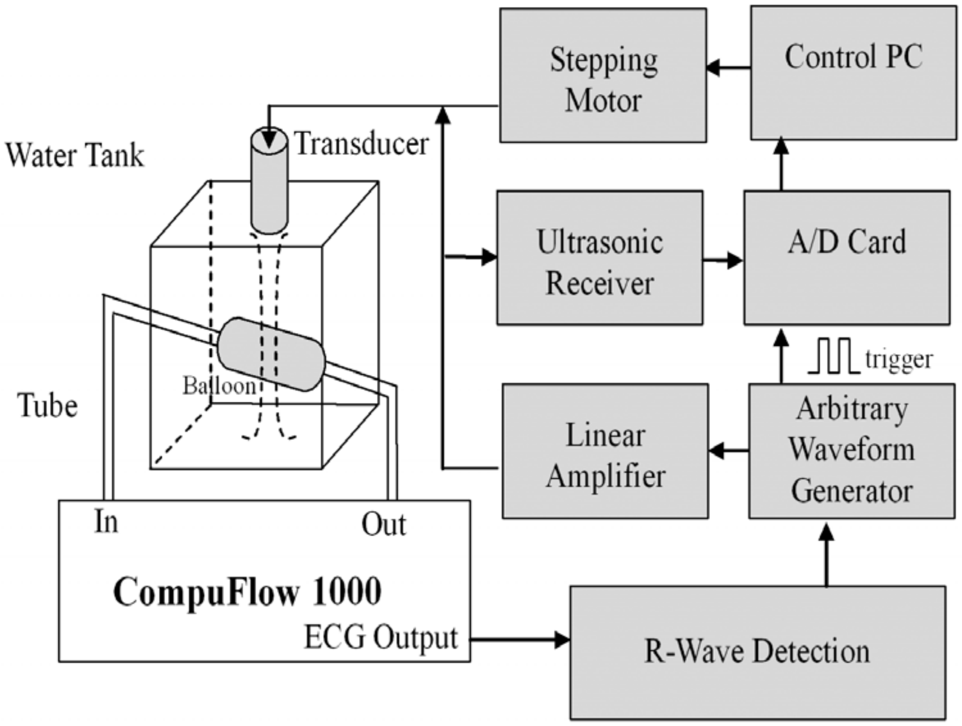

Fig. 2.8 Setup for phantom experiments

2.5 In vivo experiments

The heart rate may go down lower than 400 bmp when wild type mice are anesthesia [29]. *In vivo* experiments were performed on C57BL/6 mice weighing less than 40 g.

The mice were purchased from the National Animal Center, Taipei, R.O.C., and were housed in an animal room with a controlled environment. The animals were cared for and used in accordance with the protocols approved by the National Animal Center. Each mouse was anesthetized with halothane vapor using a vaporizer system (Fluosorber, International Market Supply, United Kingdom) and then placed on a metal plate. The anterior chest was shaved and cleaned with gel to improve acoustic coupling. After anesthesia, the heart rate is between 300 to 400 bmp in our experiments.

A block diagram of the *in vivo* experimental setup is shown in Fig. 2.9 The mouse is slightly slanted and a cushion is used to facilitate easy acoustic access. Due to anesthesia inducing a gradual decrease in the heart rate, the measured heart rate is updated using the last three consecutive R-R intervals before data acquisition. The updated heart rate is then used to determine the scanning time. After the R wave is detected, the motor moves the transducer, and a pulse signal triggers the arbitrary waveform generator to transmit a chirp signal. The arbitrary waveform generator also triggers the A/D card to sample the echo signal at the same time. ECG trigger and gating techniques are implemented to reconstruct mouse heart images. The lateral resolution at 25 MHz is approximately 120 μm, and the distance between two adjacent scan lines is 100 μm. The pulse repetition frequency is set to 2 kHz. The A/D card samples and stores the echo signals until the on-board buffer (4 MB) is full.

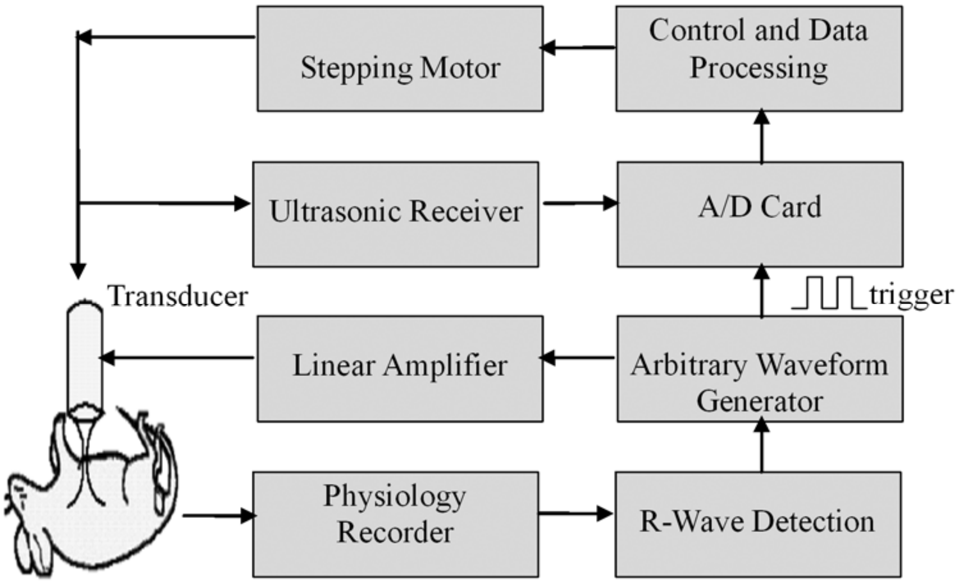

Fig. 2.9 Setup for *in vivo* experiments

2.6 The experimental results

The R-R interval in the experiments was 166±2.51 ms (mean±SD). The small standard deviation of the R-R interval indicates that the heart rate was stable when the mice were anesthetized. It is reasonable to assume that the mouse heart beat regularly and hence that both block scanning and line scanning were applicable to reconstructing ultrasonic cardiac images of the mice hearts.

Images of the balloon are shown in Fig. 2.10, for block scanning with (top panel) and without (bottom panel) ECG triggering. Fig. 2.11 is traced the upper boundary of balloon. The smoothness of the balloon boundary indicates the effectiveness of the proposed method. It is not possible without the ECG triggering or gating techniques.

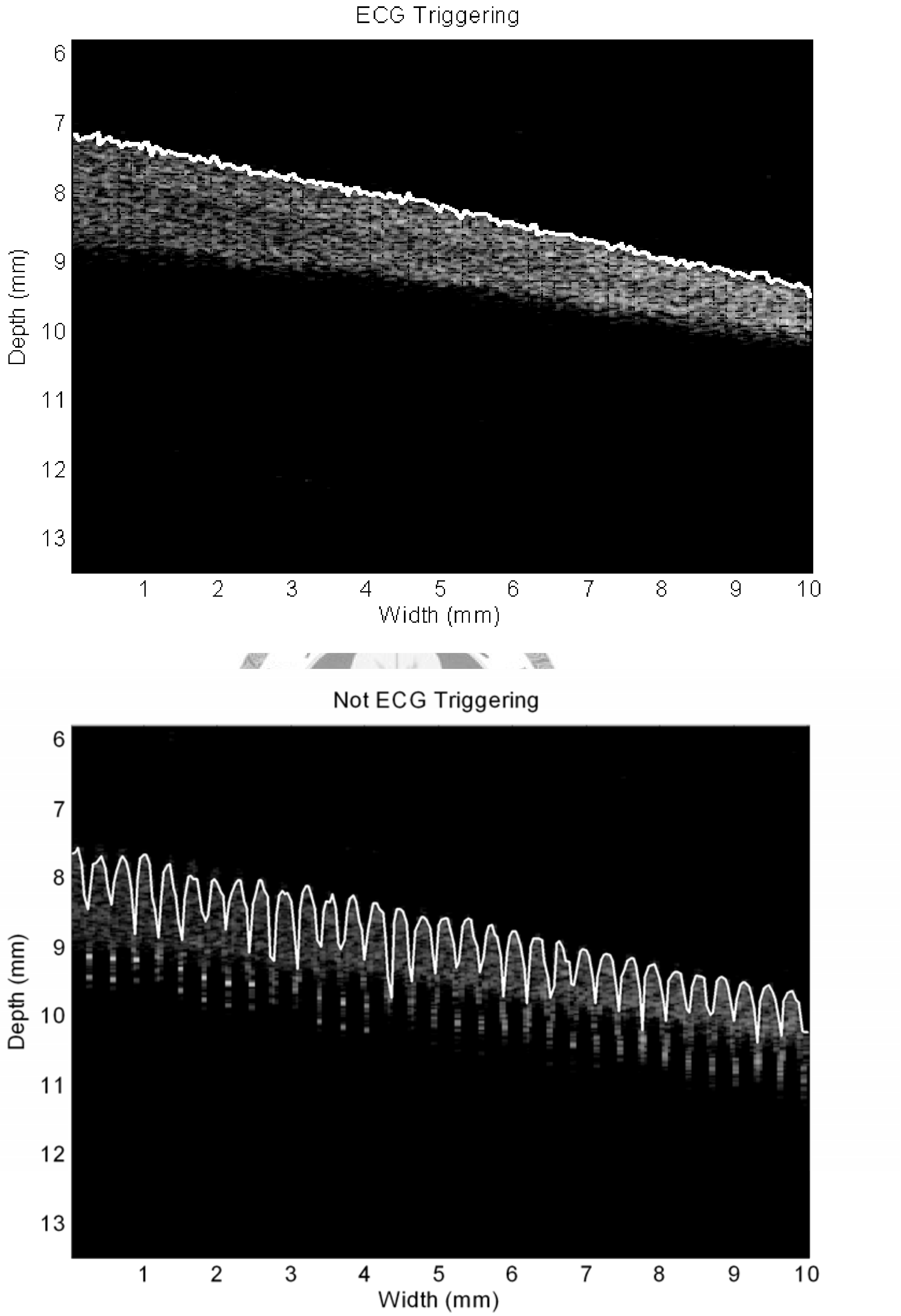

Fig. 2.10 Balloon images (top: with ECG triggering, bottom: without ECG triggering)

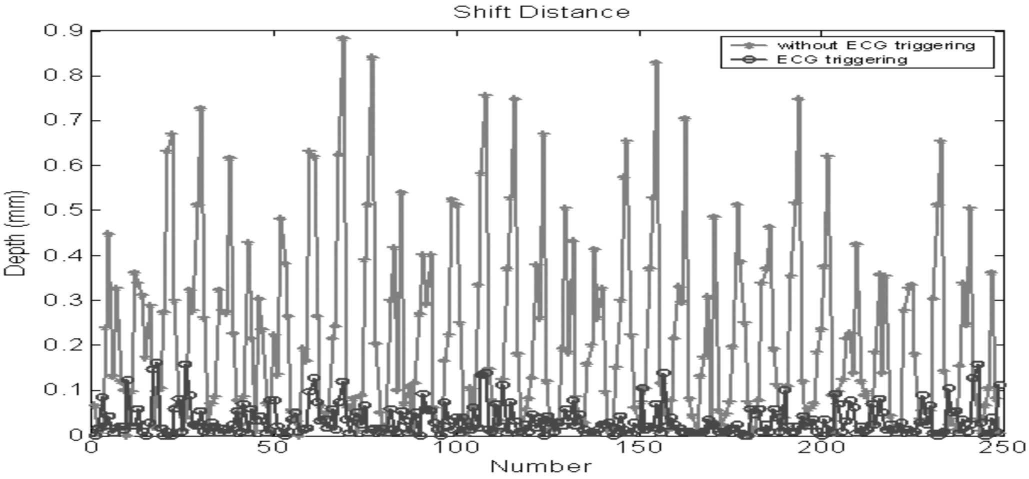

Fig. 2.11 The upper boundary of balloon

In vivo mouse images in the different cardiac phase are shown in Fig. 2.12 The motor scanning direction is along long axis of left ventricle. The endocardium border is smooth and clearly defined. LVAB and LVPB are left ventricle anterior border and left ventricle posterior border, respectively. Apex of heart and aorta are also clearly shown in every cardiac phase images. Many different cardiac phase images are manufactured to a movie file using MediaStudio Pro (Ulead, Taipei, R.O.C.,). However, without gating the temporal resolution of the imaging system is inadequate and image misalignment is clearly evident. The anatomy and dimensions of the chambers of the mouse heart can also be determined. As expected, the end-diastolic volume is larger than the end-systolic volume, making it is useful for the assessment of cardiac function. The heart volume of end-diastolic phase is shown in Fig. 2.13 The heart shape is assumed ellipse, which the long axis and the short axis are 8.1 mm and 5.3 mm, respectively. Comparison of heart size from our experiments and recent studies are similar [18]. The adult mouse heart measures about 10 mm on the long axis. Furthermore, with line scanning, M-mode images can also be acquired at all scanning positions. A typical M-mode recording of the mouse heart is shown in Fig. 2.14.

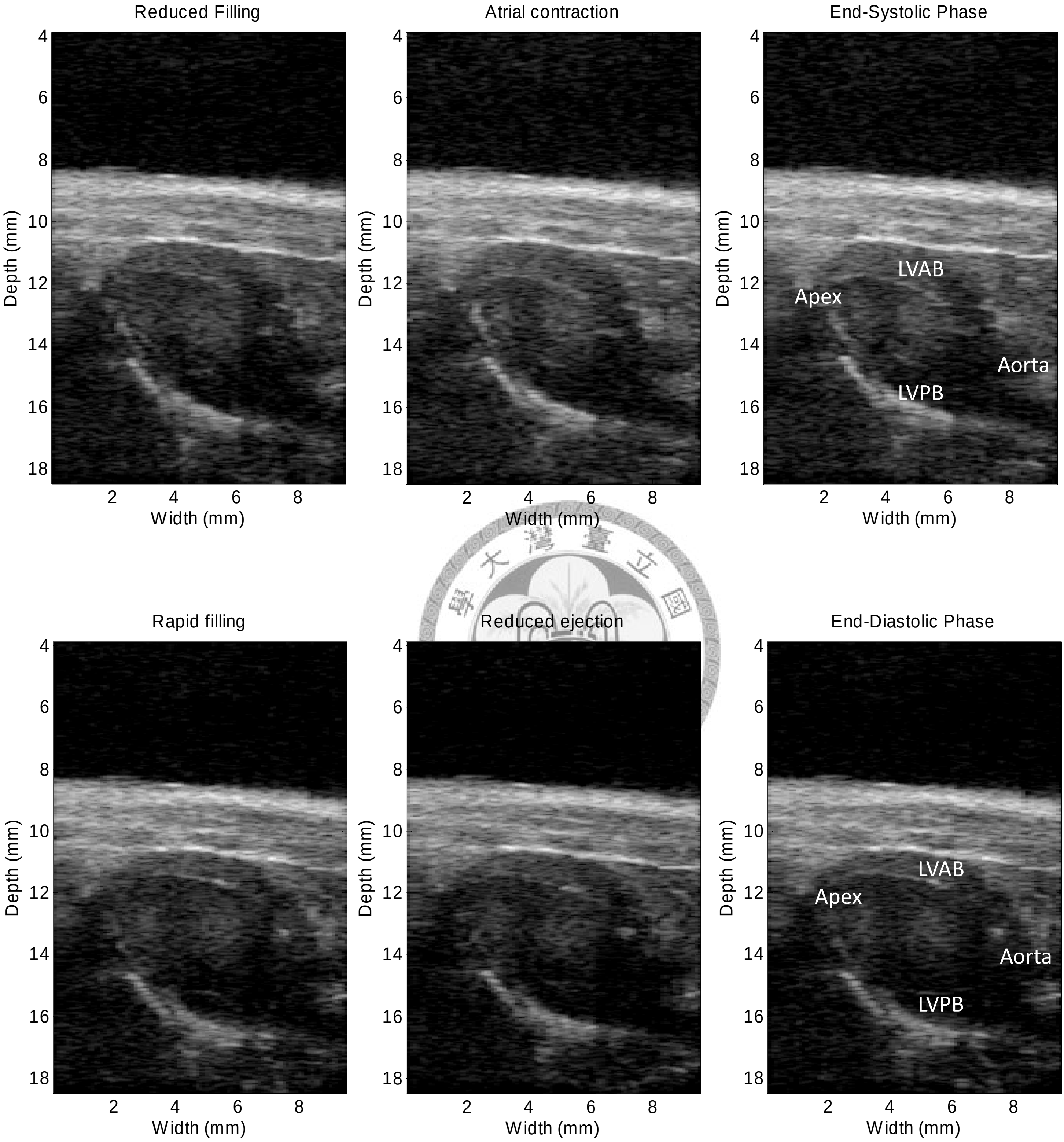

Fig. 2.12 Cardiac images in different phases

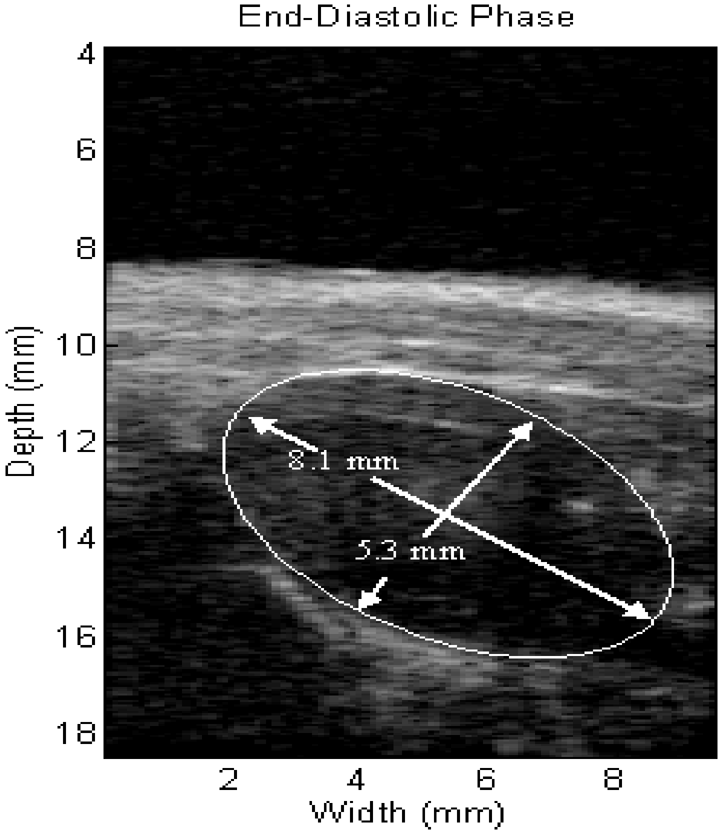

Fig. 2.13 Cardiac volume of isovolumetric relaxation

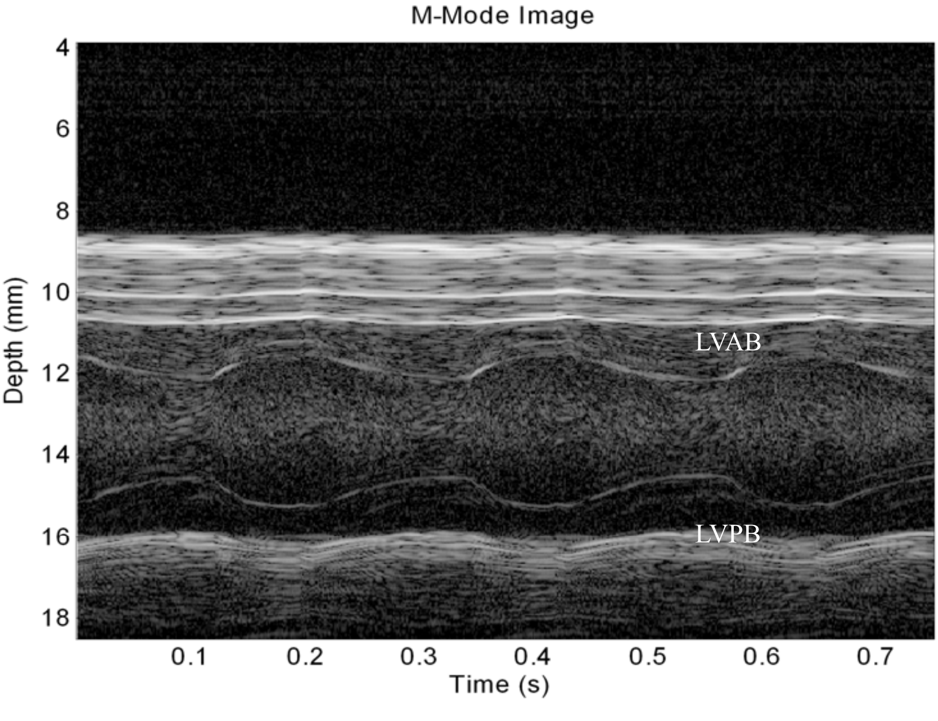

Fig. 2.14 M-mode image of the mouse heart

2.7 Concluding remarks

A high frequency cardiac imaging system for small animals was built with a spatial resolution of approximately 120 μm. Two scanning techniques were developed to minimize the motion artifacts, and their performance was verified. The block scanning mode is able to reconstruct cardiac images in the smallest number of heartbeats, but it is only suitable for obtaining images at the end-systolic and end-diastolic cardiac phases. In contrast, the line scanning mode can capture all information of the mouse heart at different cardiac phases, but it requires a longer data-acquisition time. Both methods allow the anatomy and dimensions of the chambers of a small animal heart to be evaluated. In the block scanning mode, only 7–10 heartbeats are required for image data acquisition. The effective frame rate of the system in the line scanning mode is sufficient for observing detailed myocardium motion. The techniques are also potentially applicable to other imaging modalities.

Chapter 3. Design of a High Frequency Single-Element Transducer

3.1 Introduction

Quality of ultrasonic imaging system has been improving partly due to advancements in transducer fabrication technologies. A transducer can be modeled as a three port circuit network, with two ports of mechanical ports representing the front and back surfaces of the piezoelectric material and the other one for the electrical port, representing the electrical connection of the piezoelectric material to the electrical generator [30]. In order to optimize performance of the transducer, it is important to consider mechanical-electrical energy transfer efficiency. A single element transducer includes a piezoelectric material, matching layers, a backing layer, electrodes and housing, as shown in Fig. 3.1. The most crucial component of an ultrasonic transducer is the piezoelectric material. There are a number of piezoelectric materials available. Materials such as single crystal LiNbO3 is an excellent choice for fabricating large aperture single element transducers due to the low dielectric permittivity. In contrast, material such as PZT-5H is more appropriate for array elements because of the large dielectric permittivity of the material. Furthermore, properties of other materials, which also influence performance of the transducer, also need to be considered. In this chapter, background of a single element ultrasonic transducer is presented.

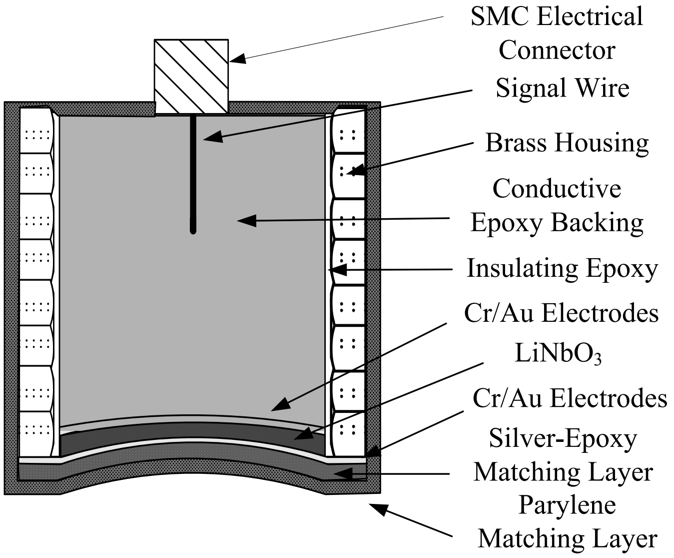

Fig. 3.1 Diagram of a single element ultrasound transducer

3.2 Piezoelectric properties

Performance of ultrasonic transducer greatly depends on the mechanical and electrical energy transfer effect. This effect, also known as the piezoelectric effect, was discovered by French physicists Pierre and Jacques Curie in 1880. The choice of the piezoelectric material is an important factor in transducer design and fabrication [31]. Several properties of piezoelectric materials are presented here, including piezoelectric constant, coupling factor, dielectric constant dielectric loss, and Curie temperature.

Many piezoelectric parameters depend on the orientation. Furthermore, stresses and strains are related to each other by elastic constants of the material in different directions. The piezoelectric material produces various stresses and strains when applied at different orientations. Conventionally, the x, y, z directions are indicated by indices 1, 2, 3 (analogous to the classical right hand orthogonal axial set) as shown in Fig. 3.2. The indices 4, 5 and 6, on the other hand, represent rotations (shear wave).

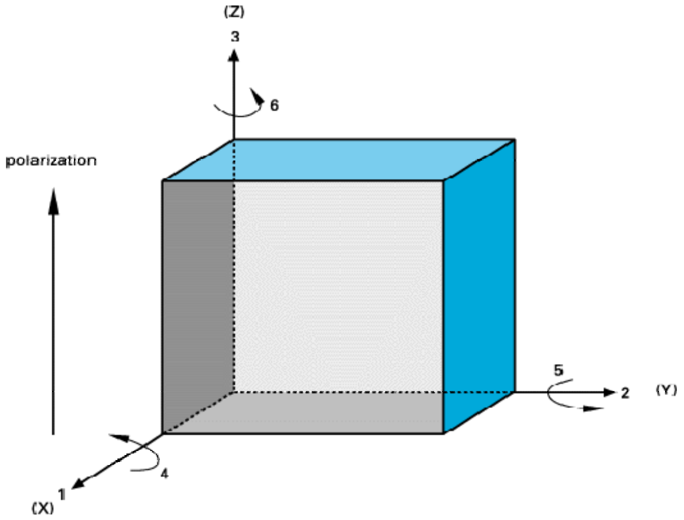

Fig. 3.2. Orientation and representation of the coordinate system

In both direct and converse piezoelectric effects, the elastic stiffness constants, c_{ij}, and stress constants, e_{ij}, are related to the electrical parameters by the piezoelectric constants, d_{ij}, g_{ij}, and h_{ij}. *For an applied voltage,* V_{in}*, the d will determine the resultant thickness change* Δt_{out}

$$\Delta t_{out} = d\,V_{in} \qquad (3.1)$$

Eq. (3.1) is used to interpret the converse piezoelectric effect. To determine the resultant voltage for the direct piezoelectric effect, two different piezoelectric constants are used. The piezoelectric deformation constant h is used to relate the resultant voltage to deformation. In this case as the thickness change, Δt_{in}, produces an output voltage according to

$$V_{out} = h\Delta t_{in} \qquad (3.2)$$

A second constant, the piezoelectric pressure constant, g is used to relate the resultant voltage V_{out} to a given applied pressure, P, given by

$$V_{out} = -(gP) \qquad (3.3)$$

The electromechanical coupling factor is related to the piezoelectric constants according to Eq.(3.4).

$$k \approx hd \qquad (3.4)$$

It is defined as the ratio of the conversion efficiency between electrical and acoustic energy. In other words, the electromechanical coupling factor is defined by the square root of the of energy ratio transforming one form into another. The coupling factor is determined using the resonance frequency. In Eq. (3.5) the resonant frequency f_r and the anti-resonant frequency f_a are used to determine the width using thickness coupling factor (k_t). The thickness coupling factor is the ratio of the stored mechanical energy in the thickness mode to the total stored energy.

$$k_t^2 = \left(\frac{\pi}{2}\right)(f_a/f_r)\tan\left\{\left(\frac{\pi}{2}\right)(f_a - f_r)/f_a\right\}. \qquad (3.5)$$

The minimum impedance frequency (fm) is the resonance frequency. The composition of the piezoelectric material and the shape and thickness of the element determine the resonance frequency. The maximum impedance frequency (fn) is the anti-resonance frequency. Maximum response of the element is somewhere between fm and fn. Values for minimum and maximum impedance frequencies can be measured by using a network analyzer. Fig. 3.3 shows the impedance response of an ultrasound transducer as a function of frequency.

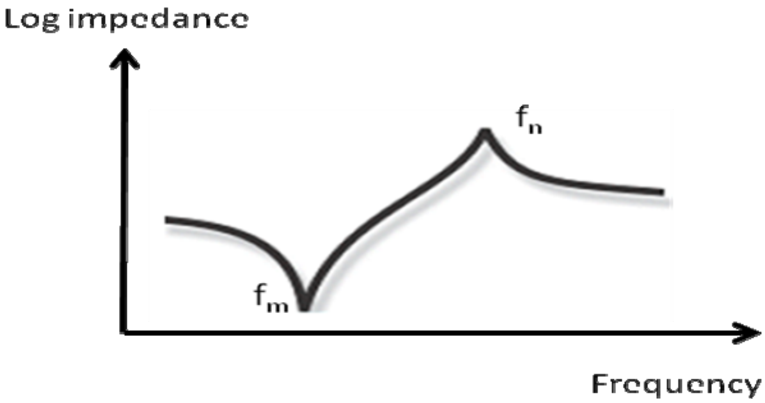

Fig. 3.3 Impedance of a typical transducer

The dielectric constant is an important factor that affects electrical impedance of an ultrasonic transducer. Electrical impedance matching is necessary between the transducer and the front end circuit. The dielectric constant is defined as

$$K = \varepsilon/\varepsilon_0 \qquad (3.6)$$

where the ε is permittivity, and ε_0 is 8.85e-12 F/m [32]. The dielectric loss, also known as the tangent of loss angle in the literature [33], is defined as the ratio of the imaginary component of the complex dielectric to its real component:

$$tan\delta = \frac{Rm\ (\varepsilon)}{Im\ (\varepsilon)} \qquad (3.7)$$

The Curie temperature is the temperature at which the piezoelectric material loses its piezoelectric properties. The Curie temperature is desired to be as high as possible to allow a large range of working temperature and must be higher than the curing temperature of the composite laminate to prevent the loss of piezoelectric properties. Practically, the working temperature needs to be 100°C lower than the Curie temperature.

3.3 Piezoelectric materials

Piezoelectric materials are available in different forms including piezoelectric polymers, ceramics, composite and crystals. The properties of common materials are shown in Table 3.1.

The polyvinylidene fluoride (PVDF) membrane is a typical piezoelectric polymer material with low acoustic impedance similar to that of human tissues and a low dielectric constant, which is suitable for electrical impedance matching. Moreover, it can be easily pressed into a curve-shaped geometry that makes excellent focusing. However, the low electromechanical coupling coefficient results in loss of signals magnitude.

The lead zirconate titanate (PZT) is a common piezoelectric ceramic material with a high electromechanical coupling coefficient which is suitable for high frequency applications. On the other hand, the large dielectric constant of PZT causes difficulties when matching the electrical impedance to the conventional 50 ohm load impedance of the electronic circuit. Due to the mediocre sound velocity, the PZT is too thin and brittle when fabricating a very high ultrasonic transducer.

The piezoelectric composite, which is combination of piezoelectric ceramic and non-piezoelectric materials, was recently developed [34]. These composites have a higher thickness coupling factor, and lower acoustic impedance which is close to the acoustic impedance of human tissue. The higher coupling factor and the better impedance matching lead to higher transducer sensitivity and finer image resolution.

The lithium niobate ($LiNbO_3$), a single crystal material, with advantages of a good electromechanical coupling efficiency and low dielectric constant, is a good choice for design an ultrasonic transducer with high sensitivity. The longitudinal sound speed 36° rotated Y Cut is high in $LiNbO_3$, which is an excellent property for a non-uniform thickness ultrasonic transducer fabrication. It is relatively easy to cut the material into different thickness for each element. Nonetheless, the high acoustic quality factor causes difficulties to make a broadband ultrasonic transducer.

Table 3.1 The properties of piezoelectric materials

Material	**K_t**	**ε**	**ρ(g/cm3)**	***C(m/s)***	***Qm***	**Z(Mrayl)**
PVDF	**0.13**	**6.5**	**1.8**	**2150**	**12**	**3.87**
PZT-5H	**0.50**	**1470**	**7.5**	**4560**	**9.2**	**34.2**
1-3 PZT	**0.6**	**200**	**3.3**	**3943**	**9.2**	**13**
LiNbO3	**0.49**	**50**	**4.64**	**7340**	**10000**	**34**

3.4 Matching layer

Performance of the ultrasound transducer can be improved by using a matching layer in the front. Ultrasonic transducers are usually designed with one or two matching layers on the face for improved sensitivity. Classical transmission line theory has been used to design a multi-stage quarter wave section impedance transformer [35]. The acoustic impedances of these layers are chosen based on the transmission line theory. By inserting a matching layer with a thickness of a quarter λ_m (the wavelength in the matching layer material) with impedance

$$Z_m = (Z_1 Z_2)^{1/2} \quad (3.9)$$

between two media with impedances of Z_1 and Z_2, the transmission in between is most efficient [37], The requisite impedances of double quarter wave layers designed for the front acoustic port are:

$$Z_{m1} = Z_1^{3/4} Z_2^{1/4} \qquad (3.10)$$

$$Z_{m2} = Z_1^{1/4} Z_2^{3/4} \qquad (3.11)$$

For wideband transducers, the KLM model, an alternative way to calculate the optimum impedance values of matching layer, has been demonstrated. Desilets, et al. [36], showed that for a single matching layer, the equation should be modified to:

$$Z_m = Z_1^{1/3} Z_2^{2/3} \qquad (3.12)$$

For two matching layers, the acoustic impedances of the two layers should be:

$$Z_{m1} = Z_1^{4/7} Z_2^{3/7} \qquad (3.13)$$

$$Z_{m2} = Z_1^{1/7} Z_2^{6/7} \qquad (3.14)$$

The acoustic impedances of piezoelectric crystals and tissues are usually close to 33 MRay and 1.5 MRay, respectively. The acoustic impedances of two matching layers are shown in Table 3.2.

Table 3.2 Acoustic impedance in transmission line and KLM medthod

	Transmission line theory		**KLM method**	
Impedance	Z_{m1}	Z_{m2}	Z_{m1}	Z_{m2}
First layer	7.0		4.2	
Second layer	14.8	3.25	8.81	2.33

3.5 Backing layer

The backing layer is also an important factor that affects performance of transducer. If air is directly on the back of the piezoelectric material, acoustic energy reflection due to acoustic impedance mismatch will arise. On the other hand, the mismatch also induces the ringing effect, causing waveform distortion and lowering the bandwidth.

The chosen backing material should not only match piezoelectric materials well but also exhibit large attenuation of the outgoing acoustic wave to damp the ringing and to increase bandwidth at a cost of sensitivity. On the contrary, the sensitivity maybe slightly detriment. The polymer resins are the commonly used material to fabricate the front and back layers a transducer. These are metal powders mixed with epoxy, such as with aluminum oxide or tungsten powders, to achieve the desired acoustic properties, including the acoustic impedance, velocity, and density [38-44]. Various ratios of aluminum oxide or tungsten powders mixed with epoxy, which fill in a container are placed in the vacuum chamber overnight. The weight of mixture is measured by a microbalance. The density is calculated by the ratio of the weight and the volume of mixture. Fig. 3.4 shows the experimental setup measuring the velocity of mixture. The transducer and hydrophone are arranged at opposite sides of the mixer. A pulser (5900PR, Panametrics) excites the transducer to generate an acoustic wave, which passes through the medium. The acoustic waves received from the hydrophone are sampled by using a digital oscilloscope (3054B, Tektronix). The velocity is measured by the difference in the time of arrival at hydrophone between the water and the mixture.

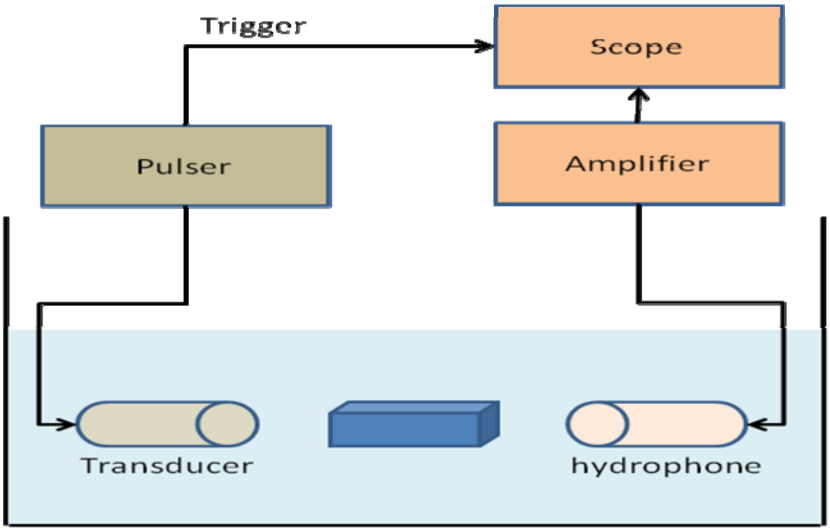

Fig. 3.4 The experimental setup for sound velocity measurements

3.6 Geometric focusing

There are two general approaches to achieve geometric focusing for an ultrasound transducer. Fig. 3.5 shows the internal focusing method (press focusing) and the external focusing method (lens focusing).

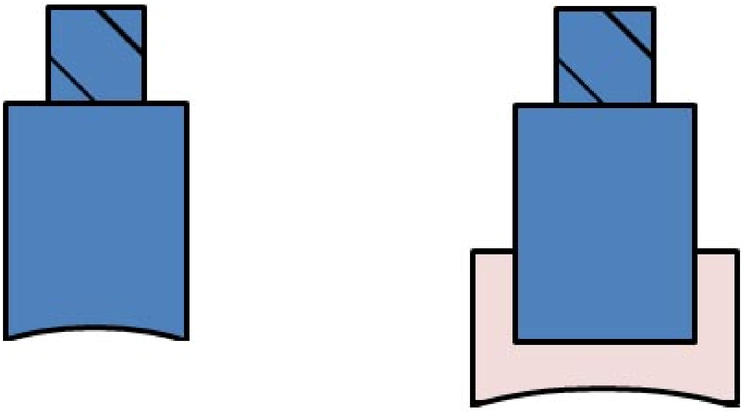

(a) (b)

Fig. 3.5 Two geometric focusing methods for the single element transducer: (a) internal focusing and (b) external focusing.

The internal focusing of high frequency ultrasound transducer is described by Lockwood et al. [45]. The focus is pressed at the surface of transducer with a steel ball. The desired focal length of internal focusing is equal to radius of curvature of the steel ball. Alternatively, when the external focusing lens is used, a formula to determine the required radius of curvature of a lens is:

$$R \cong \frac{r}{1-{}^{c_2}/_{c_1}} \quad (3.15)$$

where R is the desired focal length, r is the radius of curvature of the lens, c_1 is the sound velocity of the lens, and c_2 is the sound velocity of the load medium. Compared with internal focusing, the external focusing method provides higher bandwidth yet lower sensitivity [46]. On the other hand, manufacturing internal focusing often fails due to electrical short circuit because the piezoelectric material is broken during pressing.

3.7 Concluding remarks

Principles of designing and fabricating transducers for medical ultrasonic imaging were reviewed. LiNbO3 is an excellent choice for fabricating large aperture single element transducers due to the low dielectric permittivity and high electromechanical coupling factor. Design rules for selection of the front matching layer and the backing layer were reviewed.

Chapter 4. Design and Fabrication of a Single-Element Transducer with Nonuniform Thickness

4.1 Introduction

High-frequency ultrasound (>20 MHz) is now widely used in applications such as dermatology, ophthalmology, and small-animal preclinical studies [47-49]. These imaging systems use single-element transducers because high-frequency array imaging systems are not yet available. However, imaging systems using single-element transducers have several limitations. First, DOF is limited due to the lack of dynamic focusing. Second, the frame rate is also limited because of the need to use mechanical scanning, as opposed to the electronic scanning of an array system [50, 51]. Nonetheless, high-frequency single-element transducers are still widely used in various applications, mainly because the center frequency of commercial array transducers is limited to less than 20 MHz.

Several approaches for improving the DOF have been reported [52, 53]. One of these is to use a multielement annular transducer (MEAT) [54–56]. The structures of annualr and linear array are shown in Fig. 4.1 Compared with linear arrays, a MEAT requires fewer and hence larger transducer elements, and hence its DOF can be enhanced by electronic focusing, although mechanical scanning is still required because of the large interelement spacing still preventing the use of electronic beam steering.

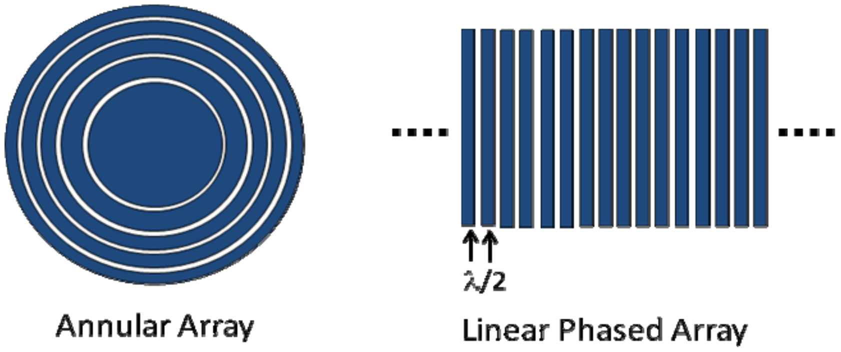

Fig. 4.1 Annular and linear array

This study reports a new type of high-frequency single-element annular transducer (SEAT). This design of transducer consists of concentric rings, where the subelements have different frequency responses due to them being constructed from different thicknesses of the same piezoelectric material. The use of a nonuniform thickness increases the bandwidth [57], and such a broadband transducer can be used to improve the axial resolution or to perform contrast and tissue harmonic imaging [58–60]. The typical bandwidth of current high-frequency transducers is around 60% [61, 62], which makes it is difficult to perform harmonic imaging. Recently an inversion-layer ultrasound transducer capable of operating over a wider frequency range has been proposed [63–66]. The inversion layer enhances the overall bandwidth of the transducer, but also reduces the sensitivity. In [63], the inversion-layer technique improved the bandwidth to 80%, with a two-way insertion loss of about 28 dB. In addition, the inversion-layer technique is difficult to implement because the annealing temperature and time of Ti film are not easy to control. The SEAT proposed in this paper represents an alternative type of high-frequency ultrasonic transducer with an increased bandwidth.

There are two major differences between the MEAT reported in the literature and the SEAT proposed in this paper. First, although the SEAT has an annular geometry, individual subelements are electrically connected and therefore cannot be individually controlled as in the MEAT. Second, all transducer elements in the MEAT typically have the same frequency response, whereas the individual subelements of the SEAT have different frequency responses so that a broader bandwidth can be achieved when they are combined. The following sections describe the design and fabrication of these transducers, and compare experimental and simulation results.

4.2 Fabrication procedures

Some of the procedures used to fabricate the SEAT are the same as those used for a single-element uniform transducer (SEUT) [61,62]. Schematics of the two types of ultrasonic transducers are shown in Fig. 4.2. The major difference between the SEUT and SEAT is in the thickness of the piezoelectric material. A SEAT was fabricated by using an electron-gun evaporator (FU-12CE, FSE, Taipei, Taiwan) to coat 10-nm-thick chrome and 100-nm-thick gold layers on one side of the piezoelectric material (36°-rotated, Y-cut lithium niobate, $LiNbO_3$) as the positive electrode. A high-attenuation material, electrically conductive adhesive (E-SOLDER 3022, Von Roll Isola, New Haven, CT), was cast on the positive electrode as the backing layer, which was thicker than 4 mm so as to reduce acoustic ringdown. The transducer was then placed in a brass housing whose inside was painted with insulating epoxy (EPO-TEK 301, Epoxy Technology, Billerica, MA) to fix and electrically isolate the transducer. The negative electrode (also comprising 10-nm-thick chrome and 100-nm-thick gold layers) was coated on the other side of the $LiNbO_3$ substrate and the surface of the brass housing. Epoxy resin loaded with metal powder was used for acoustic matching layers. The impedances of the matching layers were chosen to achieve a broad bandwidth based on the Krimholtz, Leedom, and Matthaei equivalent circuit. Silver epoxy

(EE-129-4, Epoxy Technology) was cast on the negative electrode as the first matching layer with a thickness equal to a quarter-wavelength at the primary acoustic frequency. An SMC (subminiature version c) connector was connected to the brass housing, and then the signal wire was inserted into the backing layer. Geometric focusing was achieved by pressing the transducer against a steel ball in an oven at 120°C. Finally, the deposition system (PDS 2010, Specialty Coating Systems Inc., Singapore) coated parylene-c with a thickness equal to a quarter-wavelength at the primary acoustic frequency on the transducer to make the second matching layer and waterproof.

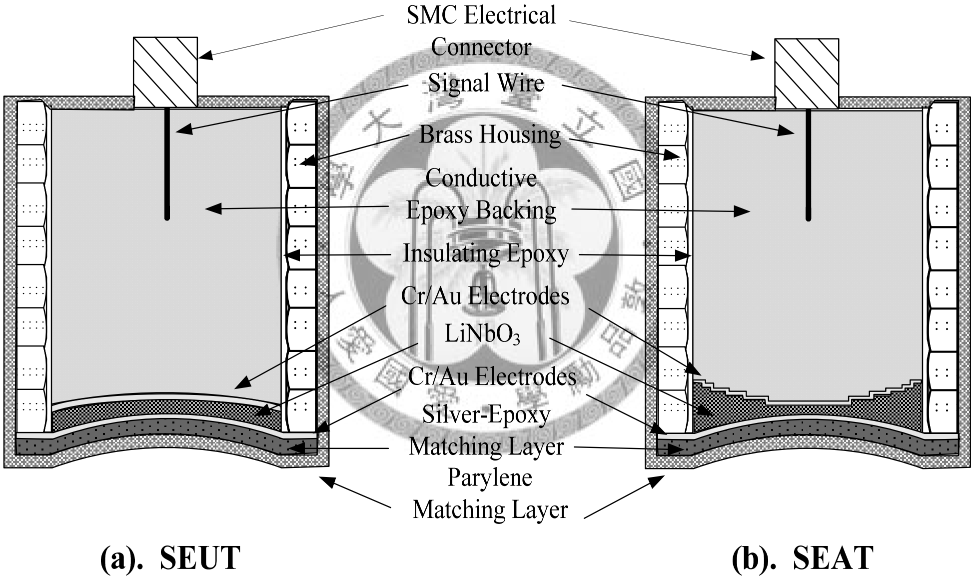

Fig. 4.2 Schematic diagrams of the SEUT (a) and SEAT (b).

4.3 Implementation of the SEAT with nonuniform thickness

Choosing an appropriate piezoelectric material is critical when designing and fabricating an ultrasonic transducer. $LiNbO_3$ exhibits good electromechanical coupling and a low dielectric constant, and hence it is a good choice for high-frequency ultrasonic transducers. The longitudinal speed of sound in 36°-rotated Y-cut $LiNbO_3$ is around 7340 m/sec, which results in a relatively thick piezoelectric material for the desired resonance frequency, thus making some of the fabrication procedures (e.g., lapping) less complicated.

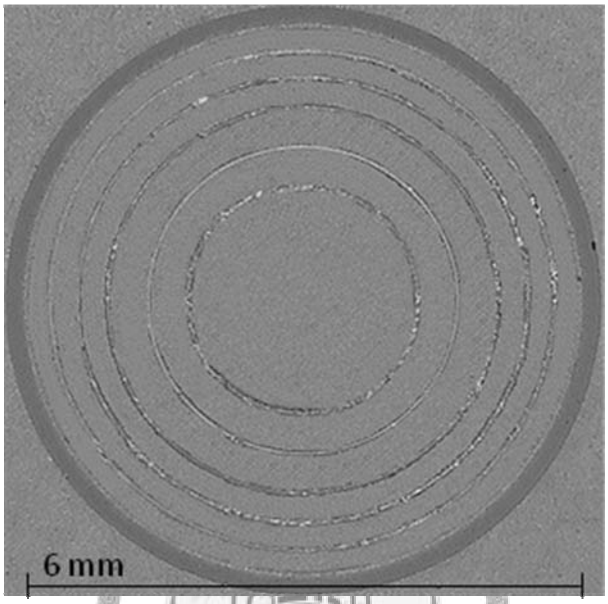

Fig. 4.3 Photograph of frontal view of the SEAT

The SEAT requires an annular geometry with concentric rings. Each ring represents a subelement, all of which have the same surface area but different thicknesses. The use of a uniform area ensures constant spectral weighting from all subelements. In our design, the $LiNbO_3$ was partitioned into six subelements with distinct thicknesses. The center frequency of the SEAT was set to 40 MHz. A smooth spectrum was obtained by keeping the difference in thicknesses between two adjacent subelements at 10 μm, which is less than 10% of the nominal wavelength. The thickness of each subelement was lower than the theoretical value (i.e., half of the wavelength at the resonance frequency) to compensate for mass loading of the matching and backing layers [67]. The diameter of the SEAT was 6 mm, and the center subelement had a radius of 1.225

mm and an area of 4.714 mm^2. Fig. 4.3 is a photograph of the frontal view of a typical SEAT, showing the six subelements with equal surface areas.

$LiNbO_3$ was obtained from Crystal Technology (Newton, MA). The fragility of this material at 40 MHz makes it difficult to implement the nonuniform thickness. An ultrasonic sculpturing machine was used in this study (Lapidary & Sonic, Taipei, Taiwan). Referring to Fig. 4.4, a laser was used to vertically align a 20 kHz ultrasonic transducer and the marble, and to confirm that the spinning disc and marble were horizontal. After alignment, $LiNbO_3$ was placed on the spinning disc that rotated continuously during sculpturing. The Wolfram steel probe was then shifted to the center of the spin disc, and the 20 kHz ultrasonic transducer continuously irradiated the 2-mm-diameter diamond powder. Note that the Wolfram steel probe did not directly touch the $LiNbO_3$ surface. The ultrasonic irradiation resulted in the diamond powders lapping the $LiNbO_3$ surface.

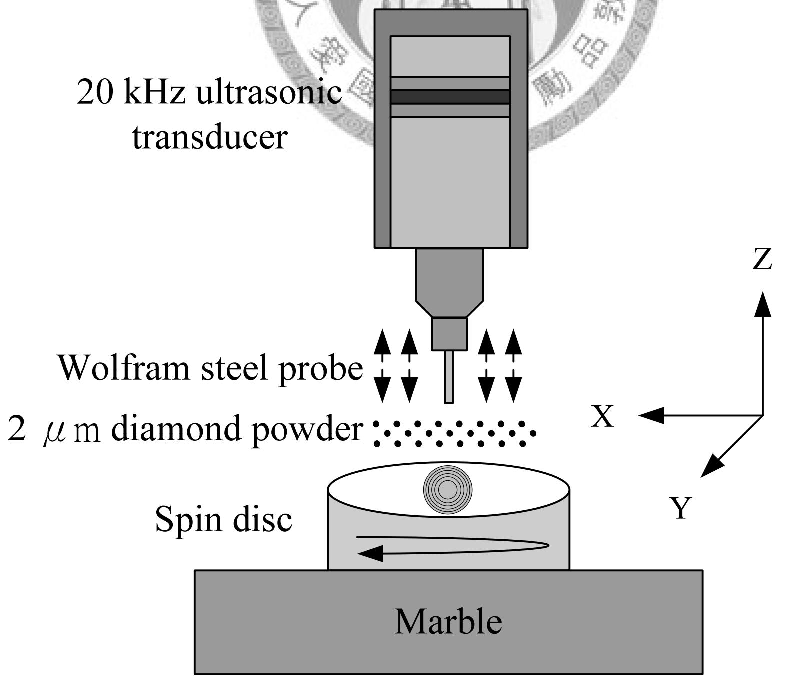

Fig. 4.4 Ultrasonic sculpturing setup.

All subelements were created using the same procedure. The x-y axial resolution of ultrasonic sculpturing machine was depended on the servo motor whose resolution is accurate in 1 mm. The z axial servo motor can easier fail in absolute position when load with a heavy object. The mechanical holder instead the servo motor to ensure the resolution at 1 mm in z the axis. The thickness ranged from center element to outer element was 60 mm to 110 mm. The range was lower than the theoretical value to compensate for mass loading of other components of SEAT [67]. The diameters and thicknesses of the annuli were verified by using high resolution microscope and length gauge (CT2501, Heidenhain Inc., Taichung, Taiwan**).** These error values were 1 m±0.5 m in practice. The results of AFM are shown in Fig. 4.5 The surface roughness of the $LiNbO_3$ was measured by an atomic force microscope (NSCRIPTOR™, NanoInk, Chicago, IL) with a conventional contact-mode probe (force constant = 0.10 N/m, Si_3N_4). After ultrasonic sculpturing, the surface roughness was measured with an atomic force microscope. The total scanning area was 2542.48 μm^2. The root-mean-square value of the roughness was 454.47 nm, which is much less than one acoustic wavelength.

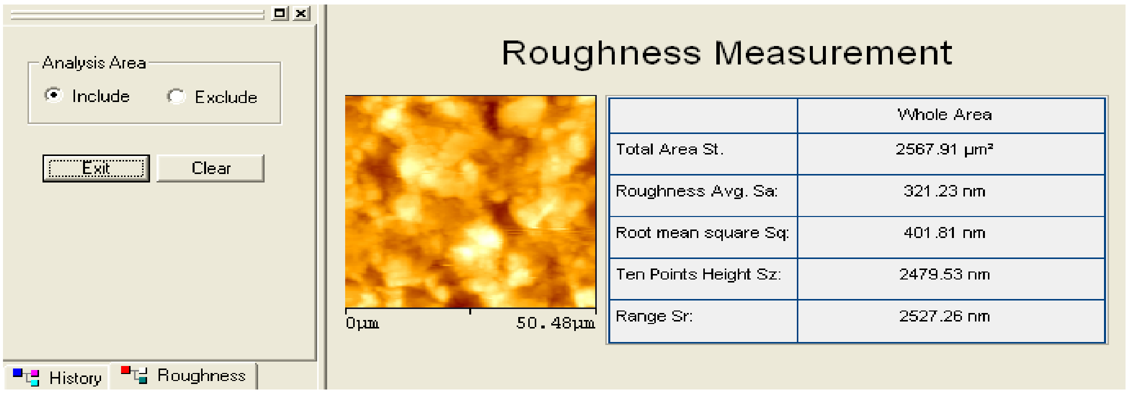

Roughness Measurement

	Whole Area
Total Area St.	2567.91 μm²
Roughness Avg. Sa:	321.23 nm
Root mean square Sq:	401.81 nm
Ten Points Height Sz:	2479.53 nm
Range Sr:	2527.26 nm

Fig. 4.5 The measurement of SEAT surface by AFM

4.4 Numerical analysis

We used a finite-element analysis software (PZFlex, Weidlinger Associates, Los Altos, CA) to investigate effects of transducer parameters and to evaluate transducer performance. The axial symmetry of the transducer was used so that a simple two-dimensional model can be used to represent the three-dimensional transducer geometry. The model consisted of six transducer subelements, electrodes, two matching layers, a backing layer, and the water interface. Properties of the 36°-rotated, Y-cut $LiNbO_3$ used in the model were adopted from [65]. The mean thickness of the piezoelectric material was set at 91.75 μm, corresponding to an operating frequency at 40 MHz. Given that the height difference between adjacent subelements was 10 μm, the thicknesses of the center and outermost subelements were 66.75 μm and 116.75 μm, respectively, with corresponding resonance frequencies ranging from 31.5 MHz to 55 MHz. Characteristics of the backing layer (E-SOLDER 3022) and the second matching layer (parylene-c) were adopted from [62]. The sound velocity and the density of sliver epoxy (EE-129-4) of the first matching layer were measured in house at 2100 m/s and 3500 kg/m^3, respectively. Thicknesses of the first and the second matching layers were set to 13.125 μm and 13.75 μm based on the quarter-wavelength criterion. At edges of the model, absorbing boundary conditions were used and infinite backing layer was effectively achieved. The SEAT was excited with a single cycle of a 40 MHz single cycle sine wave and pulse. Among the various parameters that potentially affect performance of the ultrasound transducer, here we emphasize on the effects of the driving signal and the matching layer thickness. The SEAT was excited at 30 MHz, 40 MHz and 50 MHz (both sine wave and Blackman-Harris pulse). In addition, the SEUT model with a $LiNbO_3$ thickness of 91.75 μm was also built. The excitation signals and passive materials were the same in the SEAT and SEUT. PZFlex was used to calculate beam patterns, pressure waveforms, and pulse spectra. The transmit focus was set at 10.5 mm. Because the SEAT consists of concentric rings with different frequency ranges, whereas the matching layers have a fixed thickness, the choice of the thickness is also an important issue. Using PZFlex, quarter wavelengths at 30 MHz, 40 MHz, and 50 MHz were investigated.

The results of PZFlex simulations are summarized in Table 4.1. Both a Blackman-Harris pulse (pulse envelope is the Blackman-Harris window with a duration of 1.55 cycles) and one cycle of a sine wave were used as transmit waveforms. The Blackman-Harris pulse and one cycle sine wave at 30 MHz, 40 MHz, and 50 MHz were used to excite the transducers (applied separately). The center frequency, –6 dB bandwidth, –6 dB lateral beam width, and DOF are listed in this table. The center frequency is defined as the mean frequency for which the pulse/echo spectrum exceeds –6 dB, and the DOF is defined as the axial length around the focal point where the acoustic intensity is within 6 dB of the peak. As expected, the lateral beam width and DOF decreased with the center frequency of the transmit signal. On the other hand, the bandwidth of the SEUT ranged from 52% to 62%, whereas that of the SEAT ranged from 65% to 74%. This represents a 20-25% increase in the fractional bandwidth using SEAT.

PZFlex was used to evaluate effects of matching layer thicknesses. Because the center frequency varies, the matching layer thickness can be designed to match the quarter wavelength at the center, middle and outmost subelement. The results are summarized in Table 4.2, which indicates that the matching layers should be designed for the middle subelement in order to provide the largest bandwidth.

Table 4.1. Characteristics of the SEUT and SEAT with different driving signals in the simulation.

Transducer	Driving signal	Center frequency (MHz)	Bandwidth (%)	Lateral beam width (μm)	DOF (mm)
SEUT	30 MHz Blackman-Harris pulse	36.1	52	98.8	1.2
	40 MHz Blackman-Harris pulse	40.7	57	85.4	1.1
	50 MHz Blackman-Harris pulse	42.9	59	79.4	1
	One cycle of 30 MHz sine wave	35.1	55	105	1.2
	One cycle of 40 MHz sine wave	39.	60	88.4	1.1
	One cycle of 50 MHz sine wave	40.8	62	80.6	1
SEAT	30 MHz Blackman-Harris pulse	37	65	111.6	1.4
	40 MHz Blackman-Harris pulse	42.9	68	105.8	1.4
	50 MHz Blackman-Harris pulse	45.8	65	98	1.4
	One cycle of 30 MHz sine wave	35.9	68	113.8	1.5
	One cycle of 40 MHz sine wave	41.3	78	104.6	1.5
	One cycle of 50 MHz sine wave	43.5	74	99.6	1.4

Table 4.2. Characteristics of the SEAT with different matching layer thicknesses in the simulation.

Matching layer thickness	Center frequency (MHz)	Bandwidth (%)	Lateral beam width (μm)	DOF (mm)
λ/4 for outmost element	39.3	71	107.4	1.5
λ/4 for middle element	41.3	78	104.6	1.5
λ/4 for center element	41.8	69	103.8	1.4

4.5 Acoustic measurements

Fig. 4.6 shows the experimental setup for pulse/echo measurement. The signal was reflected off a quartz plate at the focal depth in a water tank in pulse/echo mode for acoustic characterization [61, 62]. The following parameters were evaluated: center frequency, bandwidth, and two-way insertion loss. One cycle of a 40 MHz sine wave generated by a 200 MHz arbitrary-waveform generator (AWG-420, Tektronix, Tokyo, Japan) was passed through a linear amplifier (25A250A, Amplifier Research, Souderton, PA) and excited the transducer. The echoes were received by an ultrasonic receiver (5073PR, Panametrics, Waltham, MA) and digitized by an oscilloscope at 5 Gsamples/sec (3054B, Tektronix). Signals were analyzed and displayed on a personal computer using MATLAB (MathWorks, Waltham, MA).

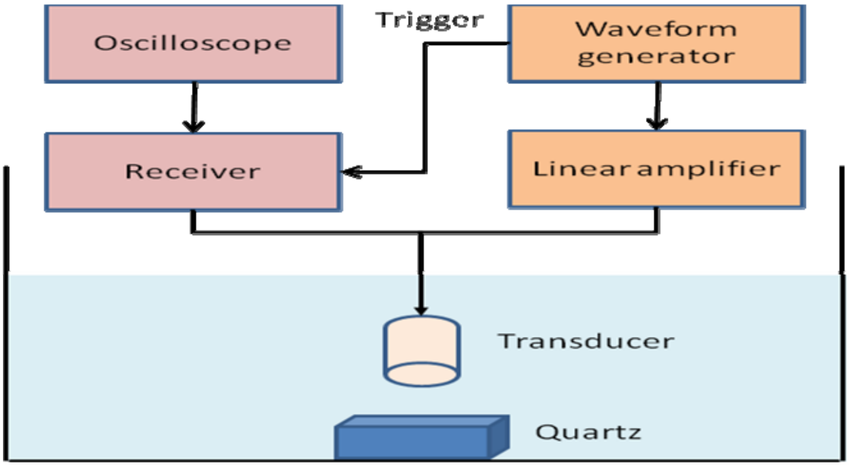

Fig. 4.6 The experimental setup for pulse/echo measurement

The acoustic beam patterns were measured using an ultrasonic beam analyzer (S-12D, Onda Corporation, Sunnyvale, CA) at a resolution of approximately 26 μm. A pulse generator (AVB2-TA-B, Avtech Electrosystems, New York) generated a 100 V mono-cycle pulse with a duration of 10 ns to excite the transducers. The pulse generator triggers the beam analyzer to capture a slice of the beam pattern. A complete beam pattern was then obtained by combining all slices obtained at different depths using delayed triggers.

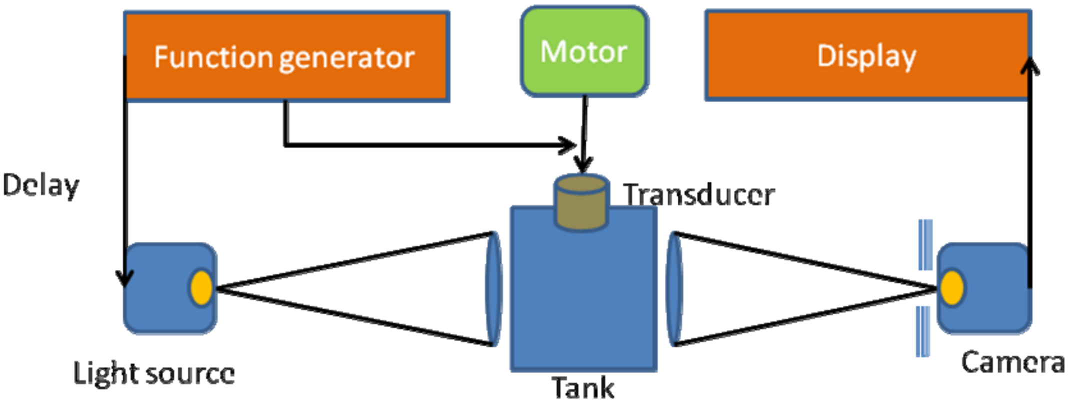

Fig. 4.7 The experimental setup for beam analyzer

A single cycle of a 40 MHz sine wave was used to excite all transducers in the experiment. The pulse/echo responses of the SEUT and SEAT are shown in Figs. 4.8 and 4.9, respectively. In both figures, the solid and dashed lines represent the experimental and simulation results, respectively. The mean center frequencies of the SEUT and SEAT are 41.3 MHz and 42.4 MHz, respectively. The –6 dB fractional bandwidths are 69% for the SEUT and 82% for the SEAT, indicating the bandwidth improvement of the latter as expected. The two-way insertion losses of the SEUT and SEAT are 16.4 dB and 19.5 dB, respectively. In other words, a 19% increase in fractional bandwidth (82/69=1.19) is gained at the expense of a 3.1 dB (19.5/16.4=1.19) degradation in two-way insertion loss. This degradation is probably due to the matching layer having a uniform thickness and therefore only matching a single frequency. The bandwidth and two-way insertion loss values of the SEUT are similar to those reported in the literature [69-70]. As a reference, a half-thickness, inversion-layer, high-frequency transducer also using $LiNbO_3$ had a fractional bandwidth of 80% and a two-way insertion loss of 28 dB [71]. Therefore, the proposed SEAT represents a good compromise between bandwidth and sensitivity.

The acoustic beam patterns measured using the ultrasonic beam analyzer is displayed in Fig. 4.10 with a dynamic range of 40 dB. The focus of both transducers was about 10.5 mm. The measured and simulated lateral beam patterns at the focal depth plotted in Fig. 4.11 for the SEUT and SEAT indicate reasonable agreement between simulations and experiments. The measured –6 dB lateral beam widths are 92 μm for the SEUT and 108 μm for the SEAT. The beam of the SEAT is slightly wider due to the aperture of this transducer being effectively apodized when excited with a 40 MHz signal, because this does not match the center frequencies of the outer subelements. This is also evident in the DOF: using the axial projection of the acoustic intensity distribution, the DOF was 2.0 mm for the SEUT and 2.7 mm for the SEAT.

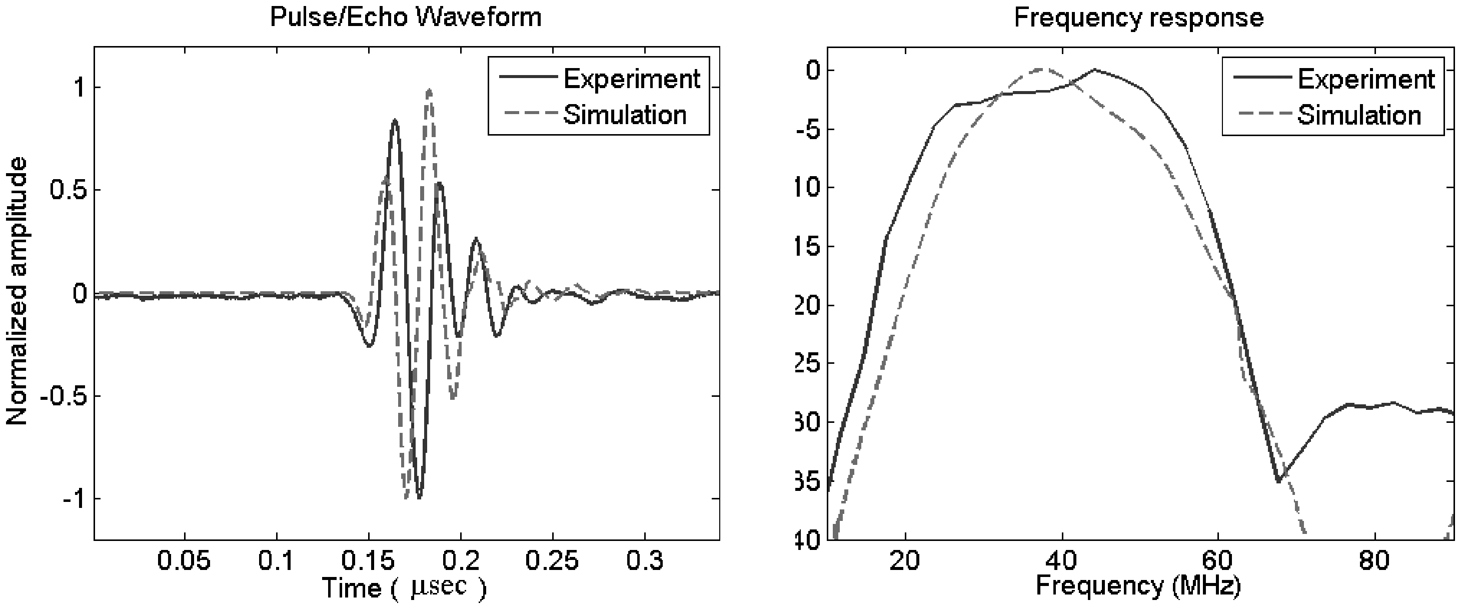

Fig. 4.8 Pulse/echo waveform (left) and frequency response (right) of the SEUT.

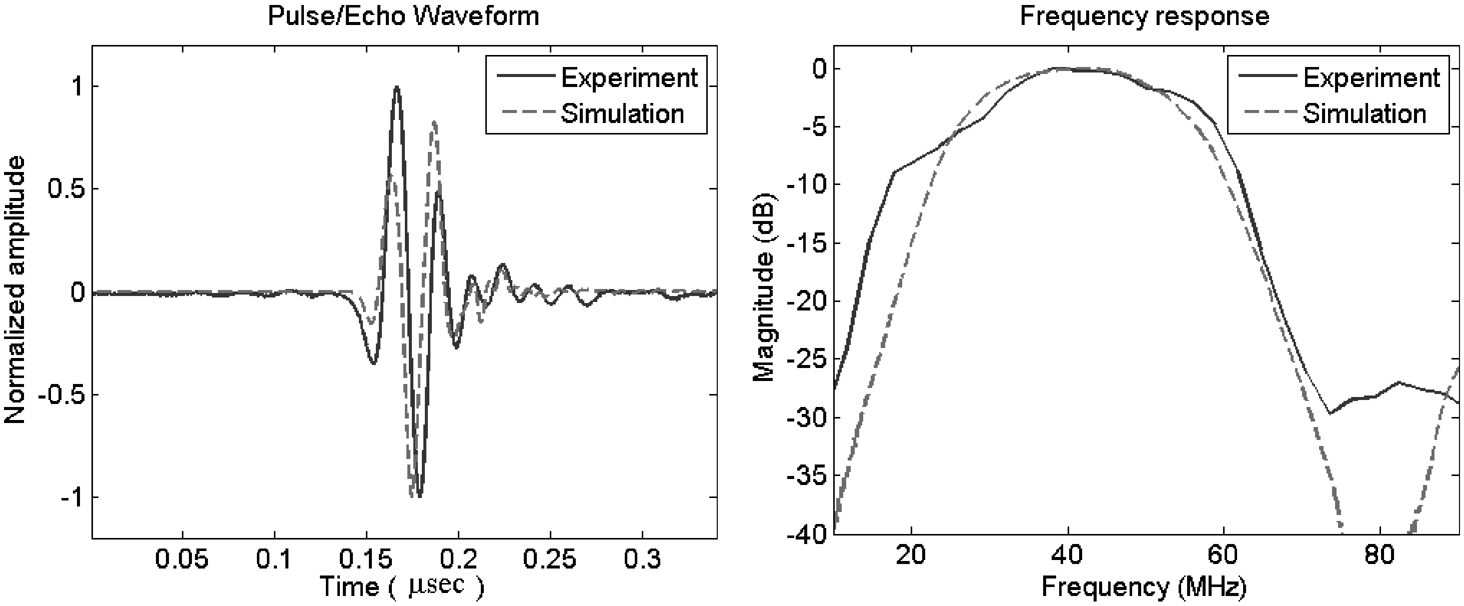

Fig. 4.9 Pulse/echo waveform (left) and frequency response (right) of the SEAT.

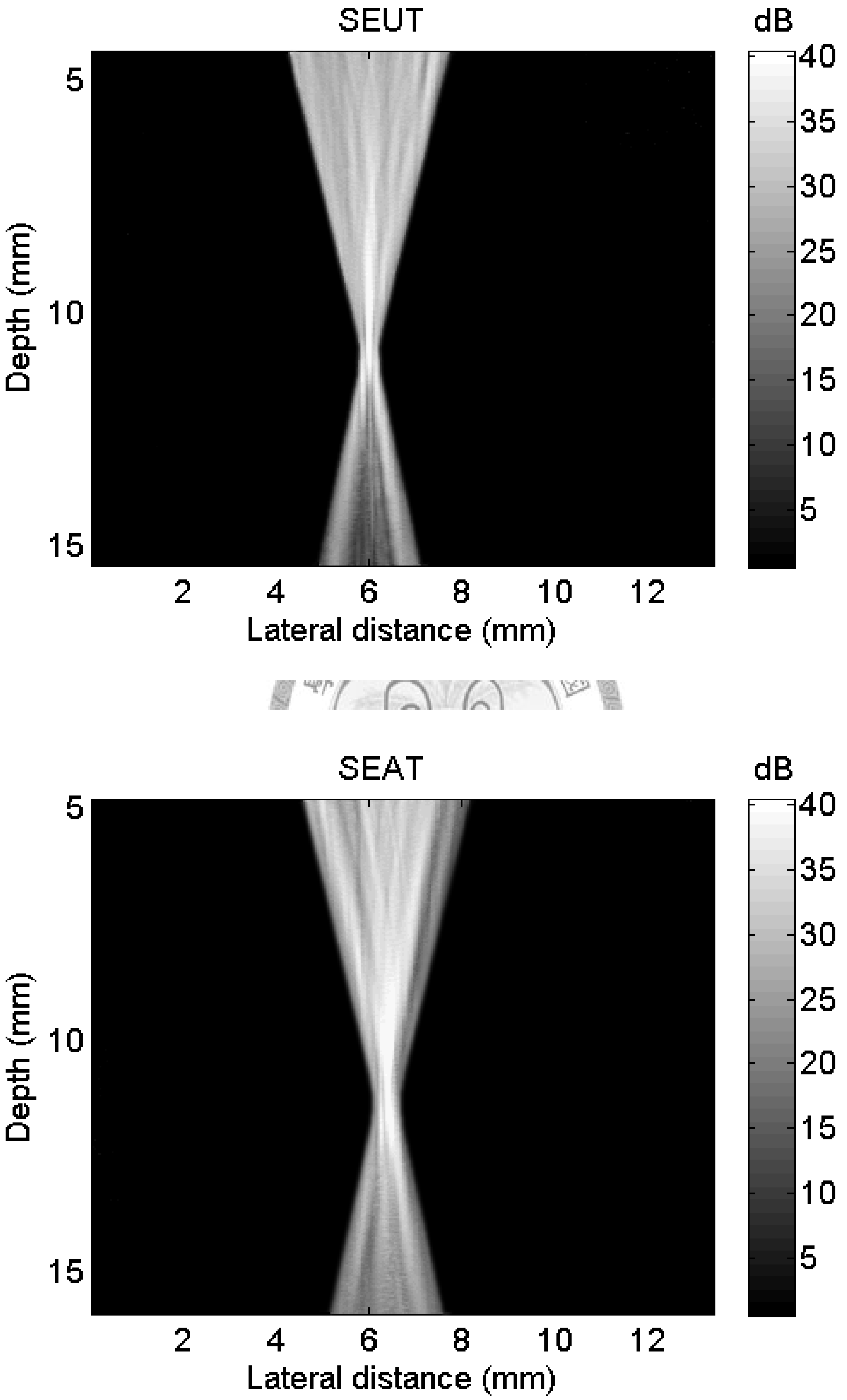

Fig. 4.10 Acoustic beam patterns of the SEUT (top) and SEAT (bottom).

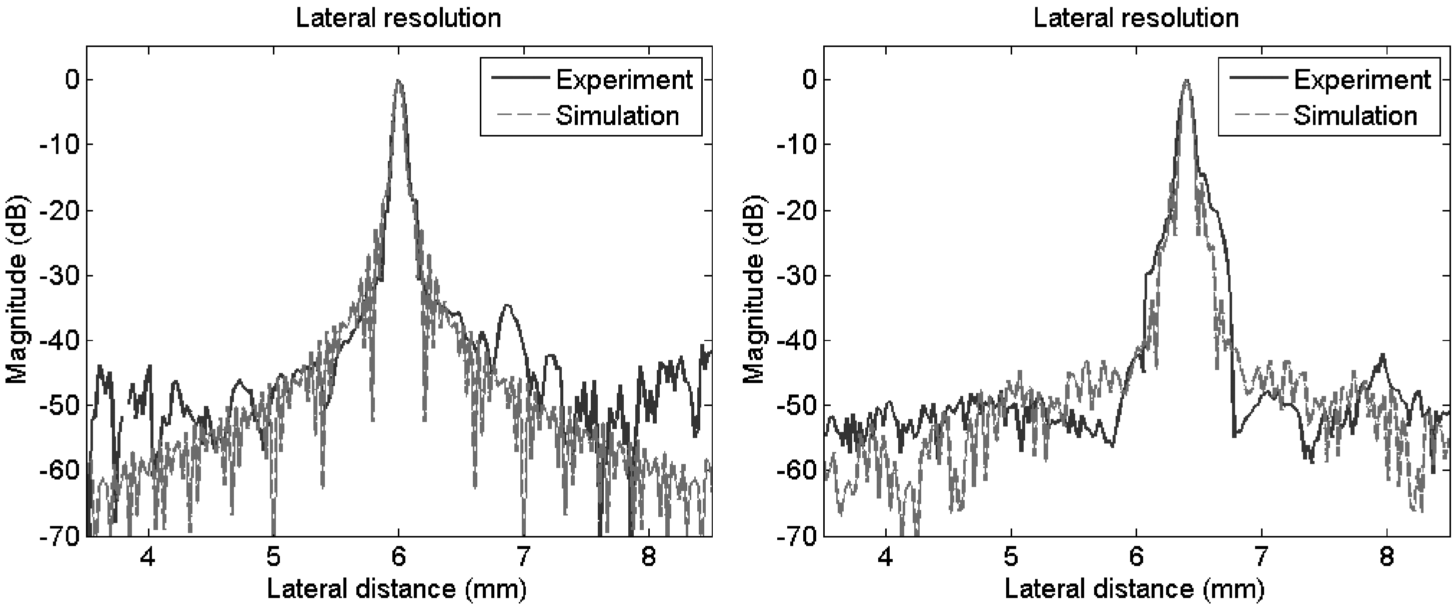

(a) (b)

Fig. 4.11 Lateral beam plots of the SEUT (a) and SEAT (b) from simulations (dashed lines) and experiments (solid lines).

4.6 Concluding remarks

Both finite-element models and fabrication procedures for the SEAT were established in this study. The driving singles and thickness of matching layers affect the performance of SEAT due to that is consisted of different particular frequencies subelements. In order to obtain the best bandwidth, lateral resolution and DOF, the driving singles and thickness of matching layers need to match the mean of overall spectrum of SEAT. The pulse/echo profiles were not in completely equivalent between experiment and simulation due to thatthe properties of materials were not enough in the finite-element model. The model can improve the accuracy by using more properties of materials such as shear velocity and attenuation of sliver epoxy, however, which are difficult to measure. The results indicated reasonable agreement between simulations and experiments. The ultrasonic sculpturing machine was able to produce a piezoelectric material with the desired thickness and acceptable roughness. Compared to the inversion-layer technique, the proposed method achieved a good trade-off between bandwidth and sensitivity. In general, the bandwidth of the SEAT was 20–30% larger than that of the SEUT, and the degradation in two-way insertion loss was also around 20–30%. Although the lateral resolution of the SEAT is affected by the aperture being effectively apodized, this apodization also provided a larger DOF. The performance of the SEAT could be further improved by applying alternative transmit waveforms (e.g., chirp waveforms) so as to apodize the aperture in different ways. Similarly, the receive aperture could be controlled using depth-dependent filtering.

Chapter 5. Design and Fabrication of a Dual Frequency Photoacoustic Transducer

5-1 Introduction

Photoacoustic imaging has been attracting research interest. It is a hybrid imaging technique that combines higher optical contrast and is less susceptible to optical scattering. A short laser pulse irradiates the tissue and causes a local temperature increase that induces an outgoing pressure wave by thermal expansion. Since the amplitude of photoacoustic waves is dependent on the distribution of the optical energy, these waves can be used to estimate the optical absorption properties of the biological tissue [72, 73].

Piezoelectric detectors [74], of which the bandwidth and sensitivity are better than that of optical detectors [75, 76], are commonly used to measure the photoacoustic signals. Most photoacoustic systems consist of a setup for light illumination and a piezoelectric detector to detect the photoacoustic signal [77, 78]. Kolkman et al. proposed a configuration using coated concentric dual ring-shaped electrodes on a polyvinylidene fluoride (PVDF) film so that the light can pass through the center surface and that the photoacoustic wave could be detected by the PVDF film [79]. The configuration of piezoelectric detector not only solves calibration problem with the optical but also improves the spatial resolution in photoacoustic scanning. However, the coating electrodes technique cannot be used to fabricate multiband detectors.

In most biological tissues, the absorbing coefficient is lower than 10cm^{-1} [80], corresponding to a peak frequency of the photoacoustic signal lower than 5MHz. The imaging resolution is therefore restricted at such a low frequency. Moreover, the depth where a photoacoustic signal can be effectively generated is limited by optical absorption and scattering properties. Therefore, photoacoustic imaging typically has smaller penetration depth than that for ultrasonic imaging. It is therefore of interest to develop a dual frequency transducer for simultaneous acquisition of both ultrasonic and photoacoustic signals at the proper frequency range. The high frequency ultrasonic signal and the low frequency photoacoustic signal can then be combined to form a multi-modality image with both good optical contrast and ultrasound resolution. Furthermore, the peak frequency of the photoacoustic signal depends on the absorption coefficient. In other words, the spectrum for a medium with a larger optical absorption coefficient is found up-shifted when compared with that with a low absorption coefficient [81, 82]. In addition to amplitude detection of the photoacoustic signal, using a dual band transducer can further enhance the contrast when the detection bands are properly chosen.

The purpose of this study is to design and develop a dual frequency photoacoustic transducer (DFPT), which also integrates an optical fiber to enable backward mode photoacoustic imaging. The DFPT consists of two concentric rings with different operating frequencies controlled by the thickness of the piezoelectric material. The design, fabrication and evaluation of the DFPT are described.

5-2 Transducer design

A schematic drawing of the DFPT is shown in Fig. 5.1. The main component of DFPT is a piezoelectric material cut into an annular pattern. The annular pattern was partitioned into two elements with distinct thicknesses corresponding to different center frequencies. Compared with other piezoelectric materials, the lithium niobate ($LiNbO_3$)

exhibits good electromechanical coupling and a low dielectric constant, therefore, it is used in this study. The longitudinal speed of sound in 36°-rotated Y-cut $LiNbO_3$ is 7340 m/sec. The high velocity is beneficial when making a high frequency transducer.

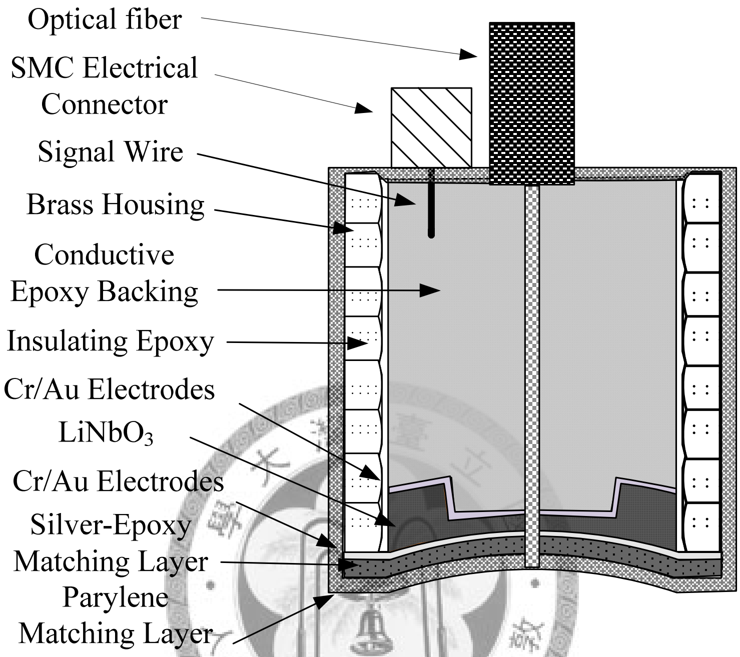

Fig. 5.1 Schematic diagrams of the DFPT.

The standard wafer of $LiNbO_3$ used in this study was purchased from TERA XTAL Technology Corp. (Taoyuan, Taiwan). An ultrasonic sculpturing machine (Lapidary & Sonic, Taipei, Taiwan) was used to make two ring elements on $LiNbO_3$ wafer. The machine generates acoustic wave, which pushes the 2-µm-diameter diamond powders to lap the $LiNbO_3$ surface. The inner and outer center frequencies of the annular ring are respectively 15MHz and 5MHz, where the difference is made by designing the thicknesses slightly lower than half wavelength of each element in order to compensate the load of matching and backing layers. The diameter of the annular structure is 6 mm, and the radius of inner and outer rings are 2.12mm and 3mm, respectively, so that the both elements have equal area. The equal area insured an equal phase shift across adjacent elements.

The thicknesses of each ring is measured by using thickness gauge (CT2501, Heidenhain Inc., Taichung, Taiwan). These thickness errors were 1μm ± 0.5μm in practice. The surface roughness of the $LiNbO_3$ was measured by an atomic force microscope (AFM, NSCRIPTOR™, NanoInk, Chicago, IL) with a conventional contact-mode probe (force constant = 0.10 N/m, Si_3N_4). The total scanning area of AFM was 2567.91 μm^2. The root-mean-square value of the roughness was 401.81 nm, which is much less than one acoustic wavelength and therefore can be ignored.

5-3 Fabrication procedures

Properties of the piezoelectric material are shown in Table 5.1. A DFPT was fabricated using an electron-gun evaporator (FU-12CE, FSE, Taipei, Taiwan) to coat 10-nm-thick chrome and 100-nm-thick gold layers on the concave surface of the annular structure as the positive electrode. A high-attenuation material, electrically conductive adhesive (E-SOLDER 3022, Von Roll Isola, New Haven, CT), was cast on the positive electrode as the backing layer, which was thicker than 4 mm so as to reduce the acoustic ringdown. The transducer was then placed in a brass housing whose inside was painted with insulating epoxy (EPO-TEK 301, Epoxy Technology, Billerica, MA) to fix and electrically isolate the transducer. The negative electrode (also comprising 10-nm-thick chrome and 100-nm-thick gold layers) was coated on the other side of the annular pattern and the surface of the brass housing. Epoxy resin loaded with metal powder was used for acoustic matching layers. The acoustic impedances of the matching layers were chosen to maintain broadband property using the Krimholtz, Leedom, and Matthaei equivalent circuit, the most efficient matching scheme. Silver epoxy (EE-129-4, Epoxy Technology) was cast on the negative electrode as the first matching layer with a thickness of 1/4 and 3/4 wavelength of the center frequencies corresponding to the inner and outer elements, respectively. Geometric focusing was achieved by pressing the transducer against a steel ball in an oven at 120°C. An 0.65 mm hole to situate the optical fiber was drilled on the surface of the transducer. A subminiature-c connector was connected to the brass housing, and then the signal cable was inserted into the backing layer. Finally, parylene-c with thickness of 1/4 and 3/4 wavelength of the respective center frequencies of the inner and outer elements was coated by a deposition system (PDS 2010, Specialty Coating Systems, Singapore) to make the second matching layer and waterproof.

Table5.1

Relevant material properties of DFPT

Piezoelectric material : 36degree Y-cut $LiNbO_3$

Piezoelectric stress constant (C m^2)			Clamped dielectric constants	
e15	e31	e33	ε33	ε11
1.54	-1.15	3.62	32.98	44.9

Radius (mm)		Frequency (MHz)		Density (kg m^3)
Inner element	outer element	Inner element	outer element	ρ
2.12	3	14.8	4.9	4460

Matching layer I	Density (kg m^3)	Velocity (m s)	Impedance (MRay)	Thickness (mm)
EPOTEK 129-4	3500	2100	7.35	105

Matching layer II	Density (kg m^3)	Velocity (m s)	Impedance (MRay)	Thickness (mm)
Parylene	1100	2350	2.585	117.5

Backing layer II	Density (kg m^3)	Velocity (m s)	Impedance (MRay)	Thickness (mm)
E-Solder 3022	3200	1850	5.92	4

5-4 Acoustic measurements

Acoustic characterization of DFPT was done in pulse/echo mode, which is done by reflecting a test signal on a quartz plate at the focal depth in a water tank. The following parameters were evaluated: center frequency, bandwidth, and two-way insertion loss.

One cycle of a 5MHz and 15 MHz sine waves generated by a 200 MHz arbitrary-waveform generator (AWG-420, Tektronix, Tokyo, Japan) were amplified by a linear amplifier (25A250A, Amplifier Research, Souderton, PA) to excite the DFPT. The echoes were received by an ultrasonic receiver (5900PR, Panametrics, Waltham, MA). Through an oscilloscope at 5G samples/sec (3054B, Tektronix), signals were analyzed and displayed on a personal computer using MATLAB (MathWorks, Waltham, MA).

The acoustic beam patterns were measured using an ultrasonic beam analyzer (HF, Onda Corporation, Sunnyvale, CA) with a resolution of approximately 26 μm. Three cycles of 5MHz and 15 MHz sine waves by the arbitrary-waveform were used to excite the DFPT. The beam pattern analyzer was triggered by the arbitrary-waveform generator. The acoustic beam was then obtained by combining all slices acquired at different depths using delayed triggers.

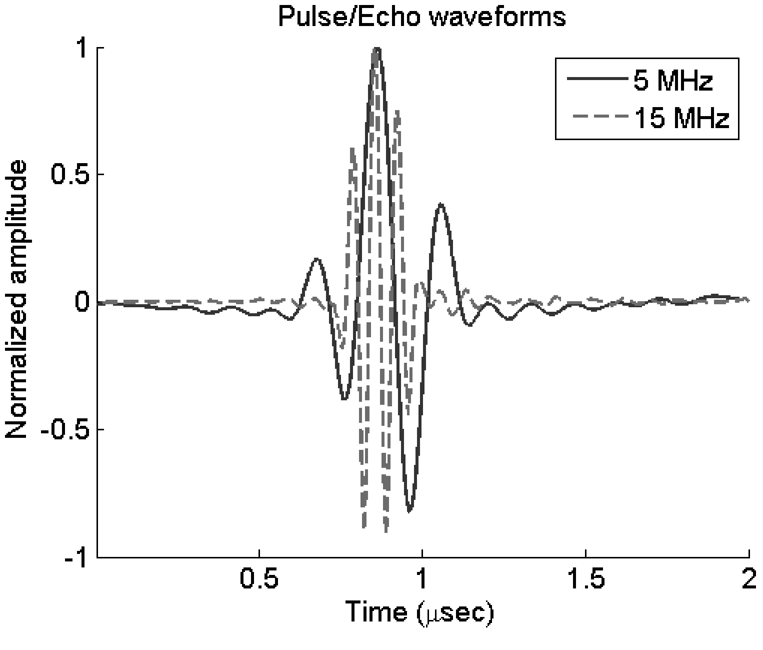

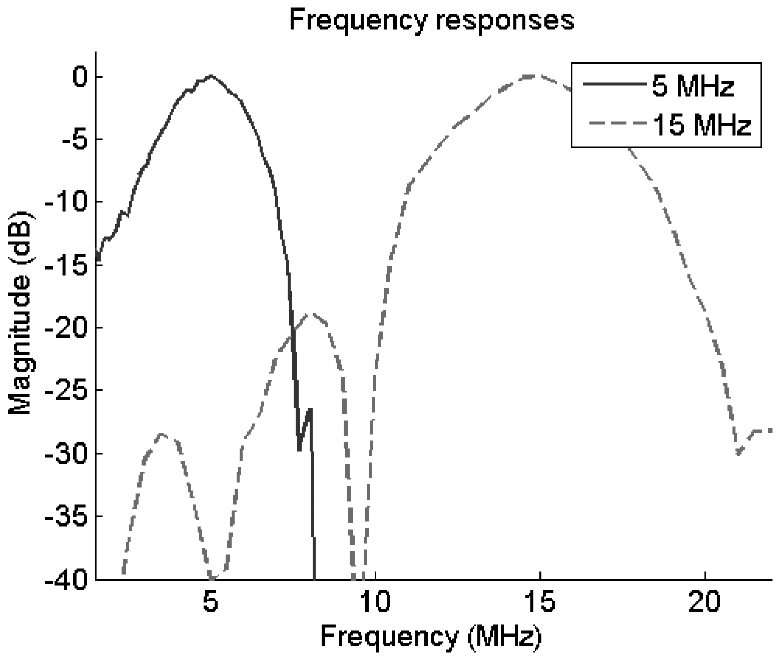

Fig. 5.2 Pulse/echo waveform (top) and frequency response (bottom) of the DFPT with different driving signals.

The center frequency is defined as the mean frequency for which the amplitude of the pulse/echo spectrum exceeds -6 dB, and the lateral resolution is defined as the lateral length around the focal point where the acoustic intensity is within 6 dB of the peak. A single cycle of 5 MHz and 15 MHz sine waves were used to excite DFPT in the acoustic experiment. The pulse/echo responses of the DFPT are shown in Fig. 5.2. The center frequencies of the DFPT with 5 MHz and 15 MHz are 4.9 MHz and 14.8 MHz. The –6 dB fractional bandwidths are 67 % and 48 % for different excitation signals. The two-way insertion loss of the DFPT is 29.3 dB. The acoustic beam patterns measured using the ultrasonic beam analyzer is displayed in Fig. 5.3 with a dynamic range of 40 dB. The Fig. 5.3 showed slight variations in acoustic beam patterns with different driving signals. The lateral projection of beam patterns at the focal depth plotted in Fig. 5.4 The measured –6 dB lateral beam widths of the DFPT are 445 μm and 275 μm, which were corresponded to excitation signals with 5 MHz and 15 MHz sine waves

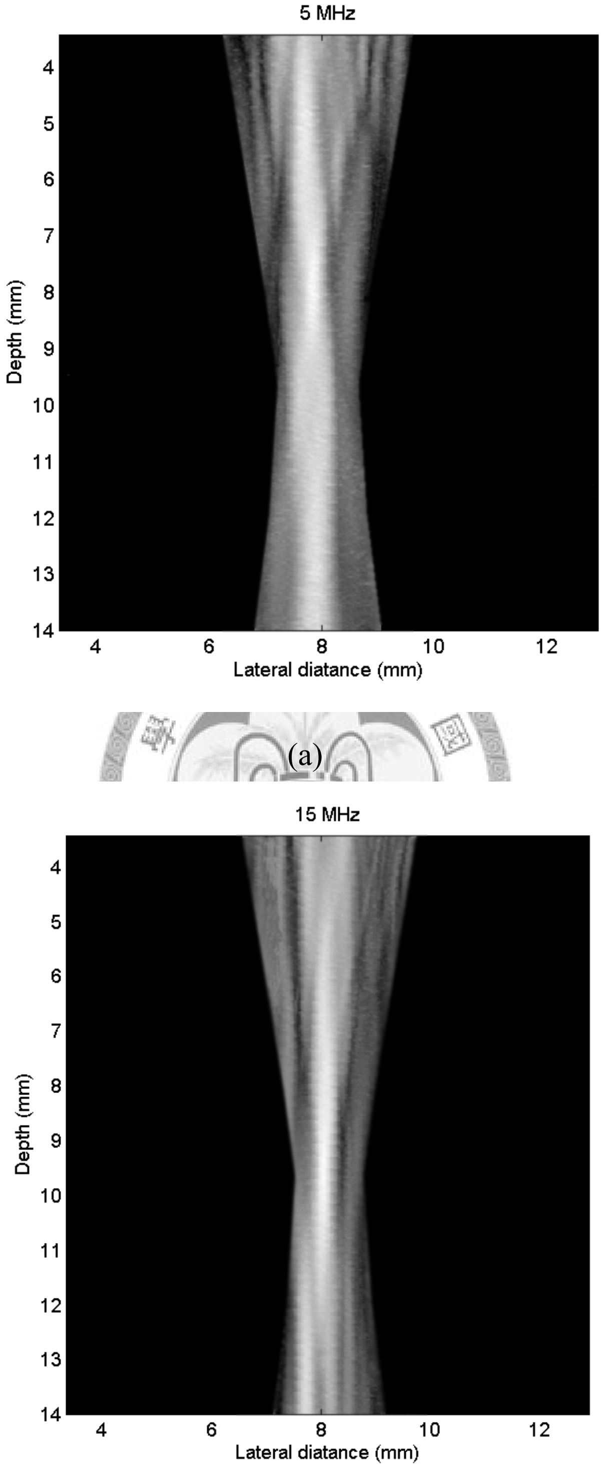

(a)

(b)

Fig. 5.3 Acoustic beam patterns of the DFPT excited by a 5MHz (a) and a 15 MHz (b) sine wave.

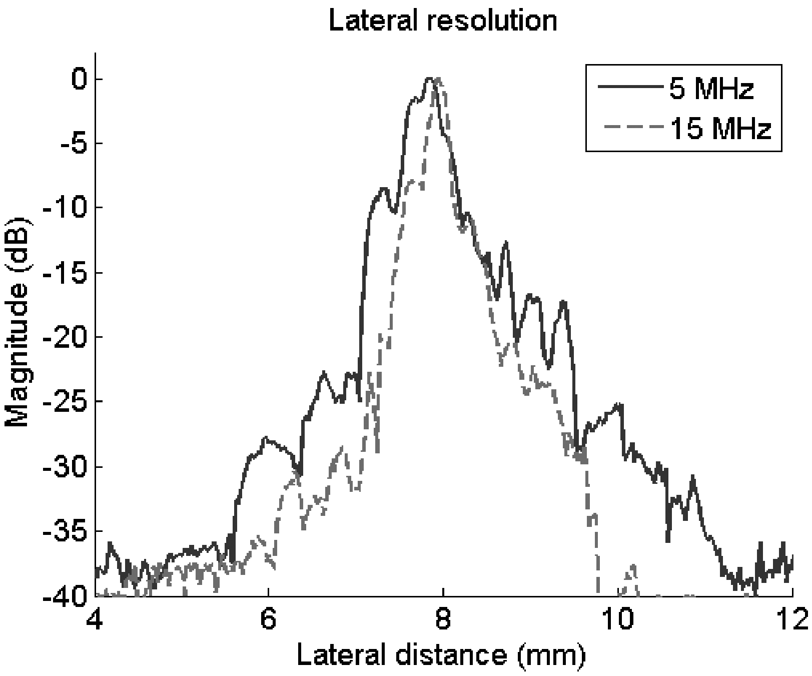

Fig. 5.4 Lateral beam plots of the DFPT with 5 MHz, and 15 MHz sine waves.

5-5 Numerical analysis

Objects with different absorption properties generate photoacoustic signals with different frequency contents. Understanding of the influence of absorption properties on photoacoustic spectral characteristics was needed to devise optimal setup for photoacoustic signal detection. Photoacoustic signal generation can be described by the thermal conduction equation, the continuity and the Navier-Stokes equations, and the state equations in the system [85]. A finite-difference time-domain (FDTD) approach is employed to solve the governing equations. To reduce computational and storage requirements, an axis-symmetrical cylindrical coordinate system with the z-axis parallel to the laser irradiation direction is adopted in our study. Moreover, the MacCormack scheme, which is fourth-order accurate in space and second-order accurate in time, and the first-order Mur absorbing boundary conditions are introduced to implement the FDTD code [86].

According to laser equipment in laboratory, the simulation of laser illumination radius is set to 3 mm, and the detection distance is 9 mm in backward direction. The time-domain results for various absorption coefficients are given in Fig. 5.5(a), and the spectrum associating with the results in Fig. 5.5(b), which are obtained by operating Fourier transform on the time-main signals in Fig. 5.5(a). Results show that the peak frequency of the signal with absorbing coefficient 5.8 cm^{-1} and 11.6 cm^{-1} are 1.1 MHz and 1.8 MHz when detected backwardly.

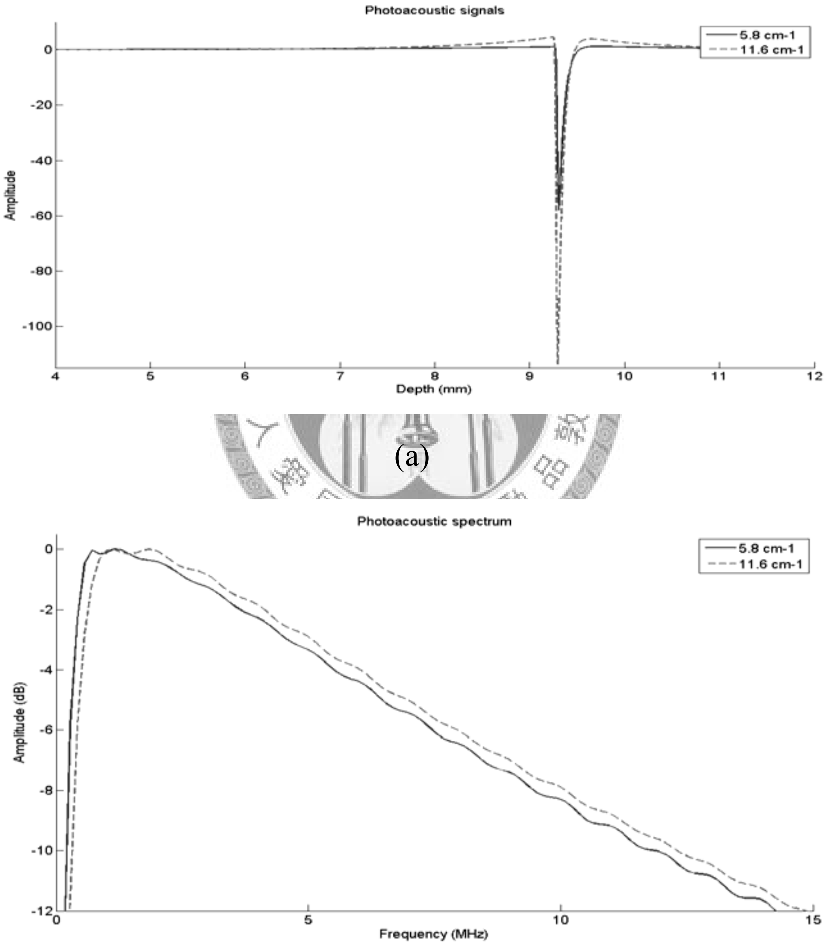

(a)

(b)

Fig. 5.5 Simulation results in (a) time- and (b) frequency- domain photoacoustic signal with different absorption coefficients.

5-6 Photoacoustic measurements

The schematic diagram of the photoacoustic experimental setup is shown in Fig. 5.6. Pure 2 % agarose (0710, Amresco, OH) mixed with 106-μm-diameter glass beads (Sigma-Aldrich, MO) was used to make the phantom with the sound velocity similar to biological tissue at about 1500 m/s , and the absorption coefficient close to 0 cm^{-1} under the irradiation of a laser pulse with 532 nm. Two regions in the phantom were stained by ink such that the absorption coefficients of about 5.8 cm^{-1} and 11.6 cm^{-1} under the 532nm laser irradiation, measured by a spectrophotometer (v570, Jasco, MD).

A Nd:YAG laser (LS-2132U, LOTIS TII, Minsk, Belarus) operating at 532 nm with a pulse duration of 5 ns was used for optical illumination. The pulse repetition rate was 15 Hz. The laser beam was coupled into a fiber (FL22-550-Multimode, ThorLabs, Newton, NJ) to irradiate a round light area of diameter about 3 mm. The irradiated laser energy density was 0.95 mJ/cm^2. The DFPT was used for photoacoustic signal detection. A precision translation stage (CSR200, CSIM Corp. Taipei, Taiwan) controlled by a personal computer was used for scanning image. The acoustic waveforms were amplified by an acoustic amplifier (5900PR, Panametrics, Waltham, MA) and then captured by a data acquisition card (CompuScope 14200, Gage, Lachine, QC, Canada) at a rate of 200M samples/sec. The acquired data were stored in a personal computer for subsequent data analysis.

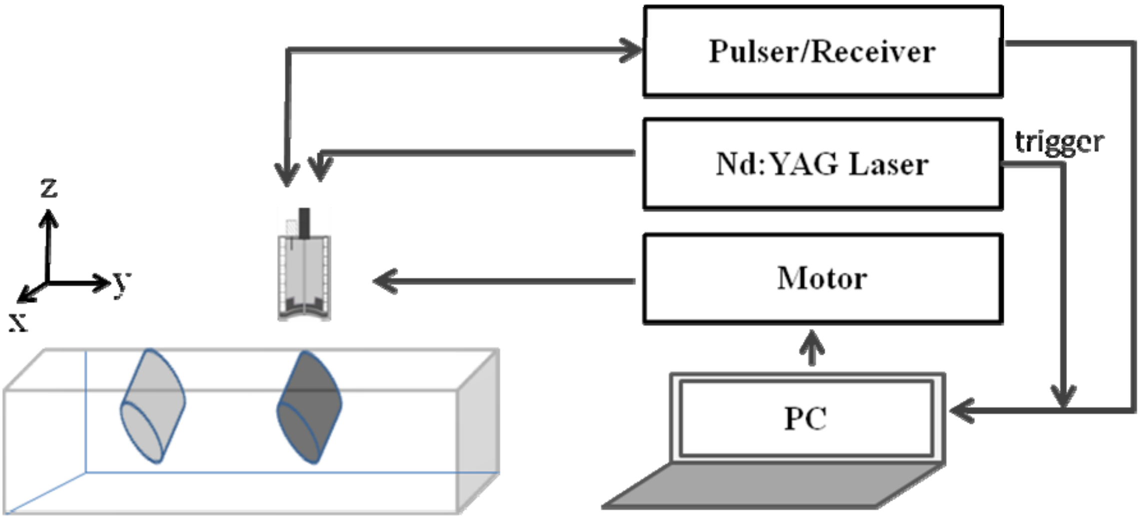

Fig. 5.6 Diagram of the experimental setup

In the experiments, the photoacoustic profiles received in backward mode and the frequency spectrums are shown in Fig. 5.7. In Fig. 5.7(a), the amplitudes of the profiles increase with the absorption coefficient. Note, the waves differ not only in intensity but also in waveform. In the frequency spectrums in Fig. 5.7(b), the photoacoustic signals with higher absorption coefficient have a larger peak frequency and a broader bandwidth. The peak frequency of the signal with absorbing coefficient 5.8 cm^{-1} and 11.6 cm^{-1} are 3.1 MHz and 3.6 MHz, respectively. In the experiment, the profile of photoacoustic signals could be dispersive, as a result from the glass beads. The trend of results in the simulation and experiment are similar, despite the differences in profiles and spectrum.

Fig. 5.8(a) shows the photoacoustic images of two agarose phantom with absorption coefficients of 5.8 cm^{-1} and 11.6 cm^{-1}. Three equal areas, the two absorbers and the background, were chosen to evaluate the mean amplitudes, which are -11 dB, -14 dB and -44 dB, respectively. A Gaussian filter with band-pass of 10-20 MHz chosen accordingly to Fig. 5.7(b) designed by MATLAB is applied on the photoacoustic signals to obtain a subband photoacoustic image (Fig. 5.8(b)). Compared with the original image, the mean amplitudes of subband image on the same locations are -15dB, -21dB and -34dB. The subband photoacoustic image demonstrated the effectiveness of contrast enhancement between different absorbers.

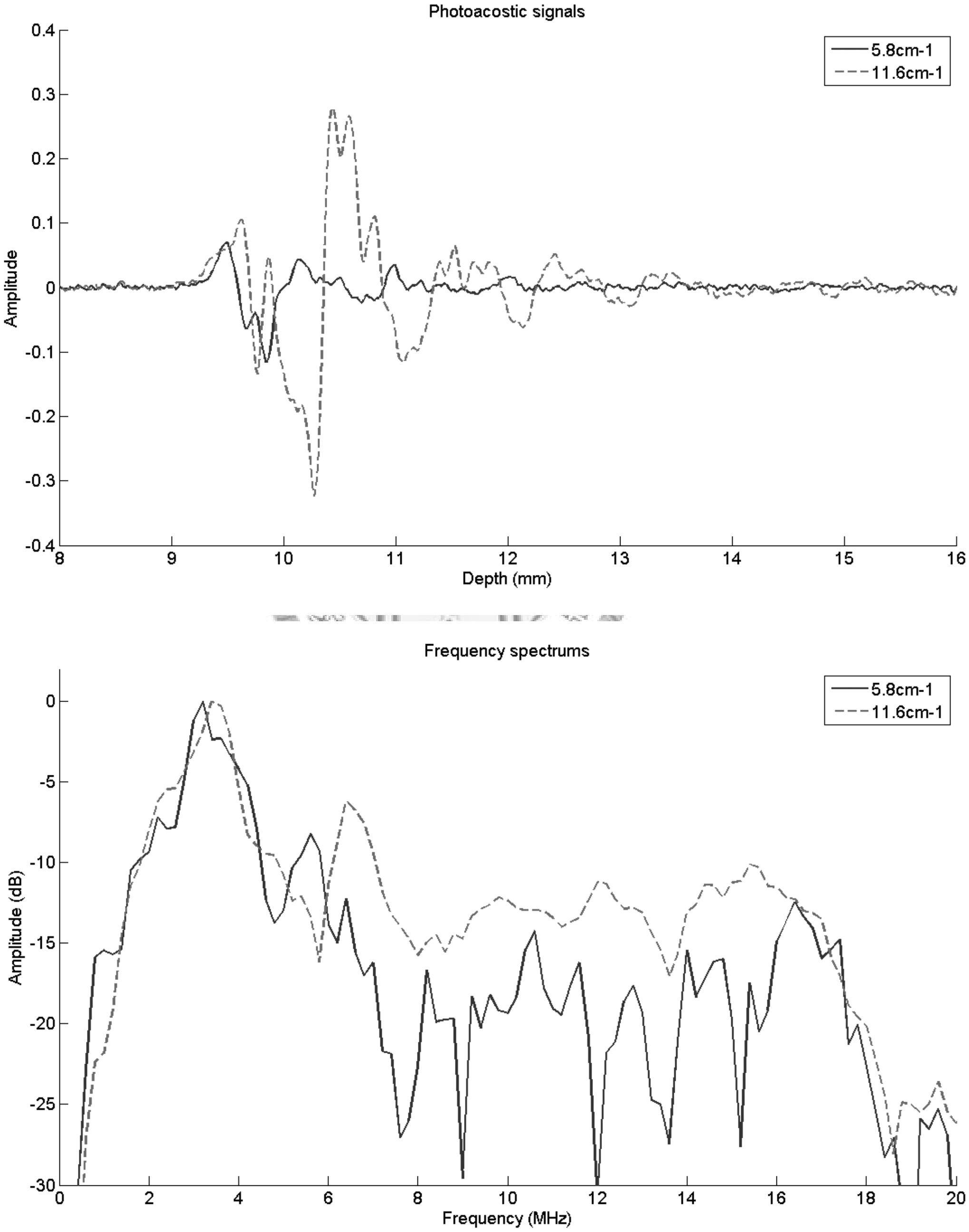

Fig. 5.7 Time domain (top) and frequency spectrums (bottom) of the photoacoustic signals detected by DFPT.

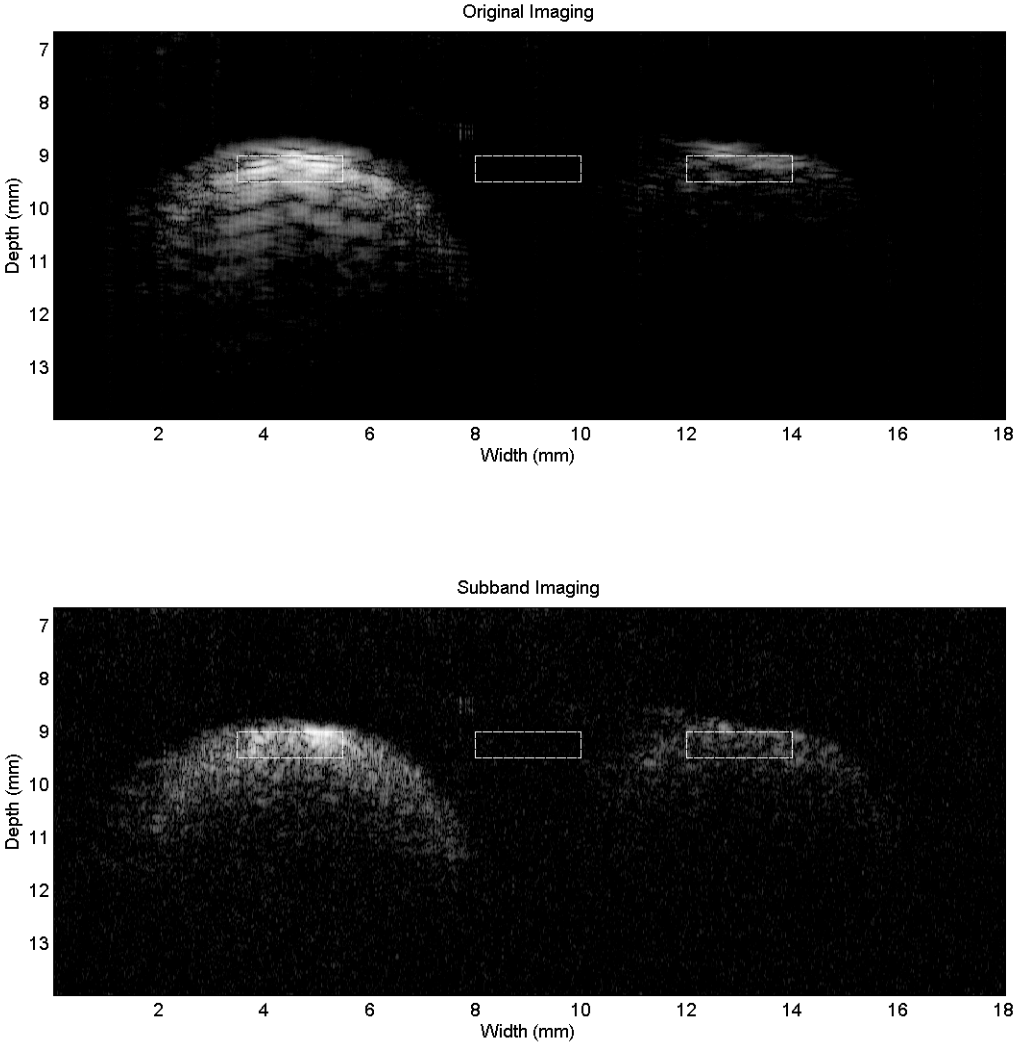

Fig. 5.8 Original (top) and filtered (bottom) photoacoustic images with absorption coefficients 5.8 cm^{-1} and 11.6 cm^{-1}

The lateral projections of the original and subband images are shown in Fig. 5.9, which can further justify the contrast enhancement. In Fig. 5.9, the difference of the mean amplitude of the two absorbers was 0.5 dB at band 5 MHz, while the difference increases to about 5.9 dB at band 5-15 MHz. The results indicate that using a relatively high frequency band, appropriately chosen according to the spectrums, the contrast between absorbers can be effectively improved.

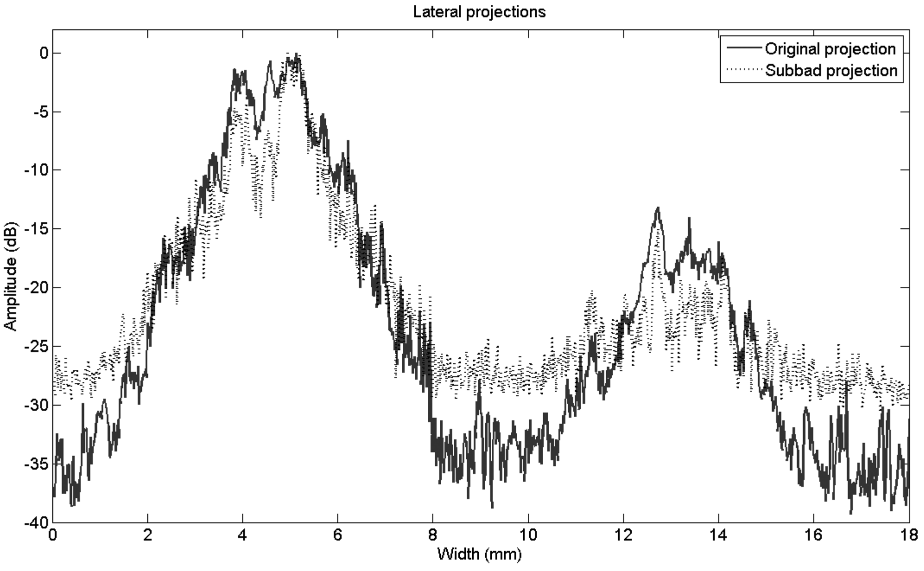

Fig. 5.9 The lateral projections with original and subband images

The acoustic signals were filtered by a Gaussian filter, with a center frequency of 15 MHz and the bandwidth approaching 80 %, to obtain the acoustic subband image. Fig. 5.10 shows the combination of acoustic and photoacoustic images with both good ultrasonic resolution and photoacoustic contrast.

5-7. Concluding remarks

A dual band photoacoustic detector was successfully fabricated in this study. Compared with the conventional detector, the DFPT is inherently confocal. The DFPT combines good ultrasonic spatial resolution and optical contrast. In our experiments, the DFPT enhanced the contrast by 5.4 dB using the subband imaging technique.

The dual frequencies of DFPT in this study are designed to have a difference with one frequency triples another in order to use a single matching layers. The DFPT can extend to a multiband detector with various frequency subbands. Since the $LiNbO_3$ is a brittle material, the thickness difference between each element is restricted. However, the crack of the $LiNbO_3$ can be avoided by using lens-focusing, at a price of the degradation of sensitivity.

Using the DFPT, the contrast between objects with various absorptions can be enhanced by the subband imaging method. In particular, when photoacoustic contrast agents are usedc(e.g., bioconjugated gold nanoparticles), larger absorption gives rise to a photoacoustic wave with higher frequency components. The DFPT is expected to improve the image quality in such applications.

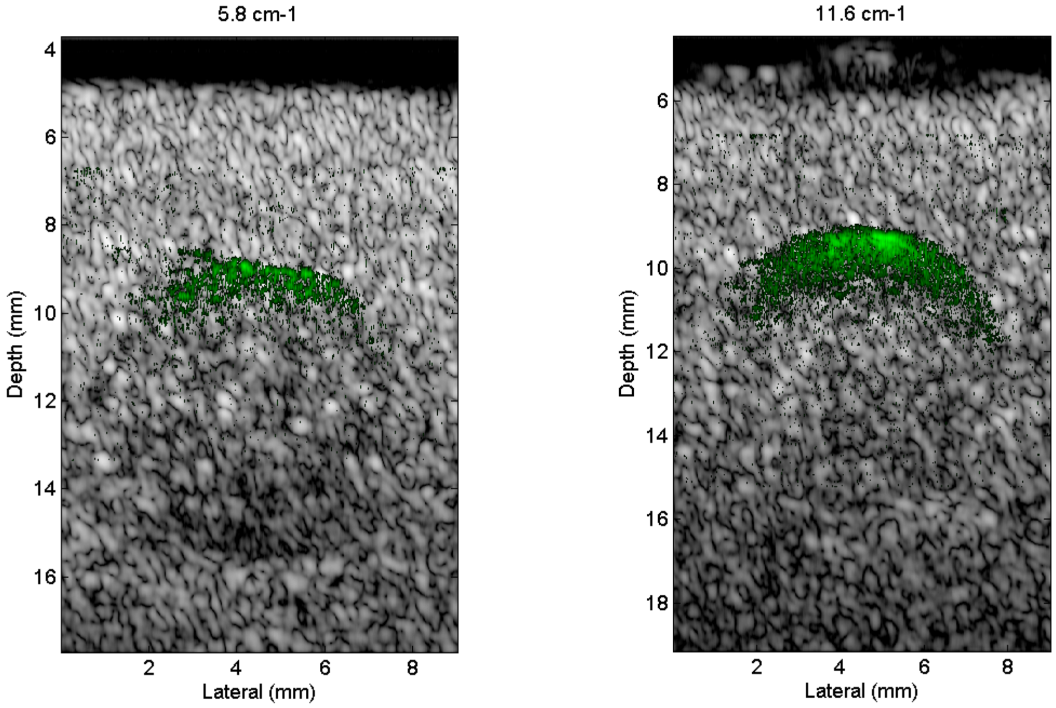

Fig. 5.10 The fusion image combining an ultrasonic image and a photoacoustic image.

Chapter 6 Conclusions

In this thesis, a high frequency cardiac imaging system for small animals was built, with the spatial resolution of the order of 100 µm. ECG gating and ECG triggering were used to effectively increase image frame rate. With these methods, heart chamber anatomy and dimensions of small animals can be determined and evaluated. Cardiac images were acquired using block scanning with the least amount of time. Line scanning, on the other hand, can obtain complete cardiac images at different cardiac phases. The effective frame rate of the system is high enough to observe detailed myocardium activities. The gating system can also be potentially applied to avoid image registration problems. In particular, integrating complementary image data from multiple imaging modalities is helpful to the comprehensive analysis of the cardiac functions and pathologies.

The principles of designing and fabricating high sensitivity and multi-band transducers for small animal imaging were also reviewed. The SEAT can provide a broader frequency range and longer DOF than the SEUT. Overall the bandwidth of the SEAT was 20–30% larger than that of the SEUT. However, the sensitivity of the SEAT was reduced by 3.1 dB compared than that of SEUT. The SEAT can be used for imaging applications that require a wider transducer bandwidth, such as harmonic imaging. The non-uniform annular pattern was also applied to develop the DFPT, which provided two frequency bands for ultrasonic and/or photoacoustic signals. It further demonstrates that the contrast between objects with various absorptions can be enhanced by using the subband imaging method. The potential to improve the contrast between biological tissues and contrast agent can also be expected.

Chapter 7 Discussion and future works

7.1 Other high frame rate ultrasonic systems

Most high frequency ultrasonic studies are carried out by mechanically scanning a single-element transducer. Unfortunately, it is very difficult to achieve the frame rate over the 100 Hz. To overcome this limitation, high frequency linear arrays with electronic scanning are desired. Several group have developed linear arrays operating at 30 MHz [87–90], but to further increase the frequency to 50 MHz is still a very challenging task. Moreover, the cost of a high frequency array system is also a major concern.

Fast mechanical sector scanner offers an interim solution. A small animal system for mouse cardiac imaging has been developed by Visualsonics (Vevo 770; Visualsonics, Toronto, ON, Canada) with the spatial resolution down to 30 μm. Although the EKV^{TM} technology promoted by Visualsonics can achieve a frame rate up to 240 Hz and can be used for quantification of physiological functions of a developing mouse heart, no technical details on the image width were available at this point. In [90], a sector scanning system was reported. In this case, a high sweep rate sector motor and a light-weight SEUT were used to achieve a frame rate up to 130 Hz.

The ECG triggering and ECG gating methods for mouse cardiac imaging can be also used to effectively increase the frame rate to over 2 kHz. At such an effective frame rate, quick moving organ can be examined in detail. However, this technique requires a long acquisition time and retrospective reconstruction is required.

7.2 Non piezoelectric device

Recent advances in Microelectromechanical systems (MEMS) technology have made non-piezoelectric devices (e.g., capacitive micromachined ultrasound transducer, CMUT) feasible [91-92]. Fig. 7.1 shows the structure of a capacitor cell, which usually consists of a metalized membrance (top electrode) suspended above a heavily doped silicon substrate (bottom electrode). An insulating layer is design to avoid shorting of the two electrodes.

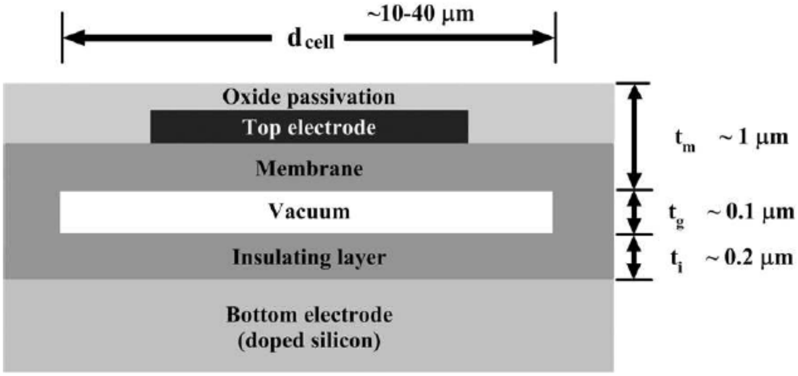

Fig. 7.1 The structure of CMUT

A single element is consisted of multiple small capacitor cells in parallel. A DC voltage is applied between the metalized membrane and the substrate during CMUT operation. The membrane is attracted toward the bulk by the electrostatic force, and induced stress within the membrane balances the attraction. Driving the membrane with an alternating voltage superposed on the DC bias voltage generates ultrasound. If the biased membrane is subjected to ultrasound, a current output is generated due to the capacitance change under constant bias voltage. The amplitude of this current output is a function of the frequency of the incident wave, the bias voltage, and the capacitance of the device. Mathematically, this relationship can be expressed as:

$$I_{AC} = V_{DC}\omega_a C_0 \frac{\Delta x}{x_0} \qquad (7.1)$$

where V_{DC} is the DC bias voltage, ω_a is the acoustic frequency, C_0 is the capacitance of the device, and $\frac{\Delta x}{x_0}$ is the fractional displacement due to the incident wave. The efficiency of CMUT is determined by the electromechanical transformer ratio, which can be expressed as the product of the device capacitance and the electric field strength across the gap beneath the membrane.

CMUT is seen as an alternative to ultrasound transducers for use in existing systems. Due to the maturing MEMS technologies, the yield rate of CMUT has also improved. It is expected that performance of CMUT will continue to improve in the future and therefore maybe a good candidate for high frequency applications.

7.3 Enhanced resolution of SEAT

The depth of fields (DOF) of SEUT is limited due to the geometry shaped for the focusing purpose. In other words, the SEUT provides the best resolution near the geometric focusing, but the performance outside the focus deteriorates. Compared with that of the SEUT, the bandwidth and DOF of the SEAT are improved. Fig. 7.2 schematically shows the relationship of center and spatial position on SEAT's surface. Due to the non-uniform thickness of the annular pattern, the SEAT can excite acoustic waves composed of different frequencies. In other words, spectral characteristic of the signals vary across the surface of the SEAT. Thus, filtering can be applied on signals received by SEAT to control the effective active aperture size and further enhance the lateral resolution in the near field. To obtain filtered images, three Gaussian filters, whose magnitude spectrums are shown in Fig. 7.3, are designed using MATLAB. These filers cover the whole spectrum of the SEAT and the SEUT.

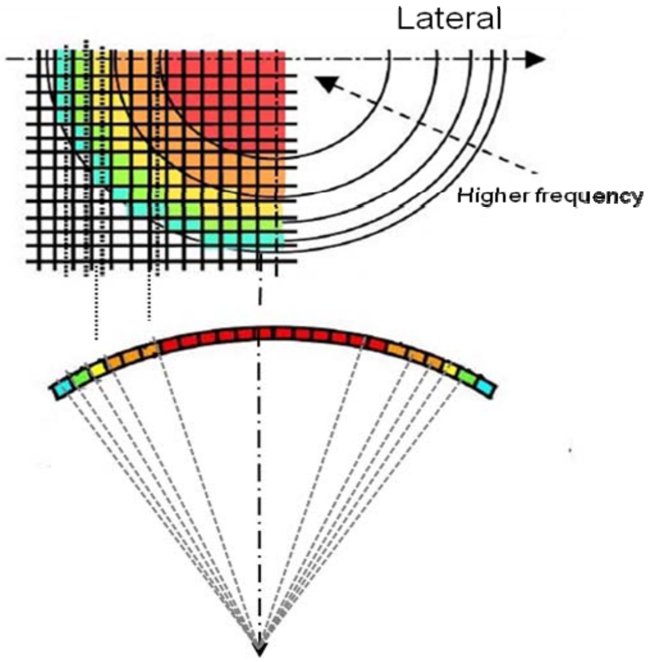

Fig. 7.2 Frequency response distribution of SEAT

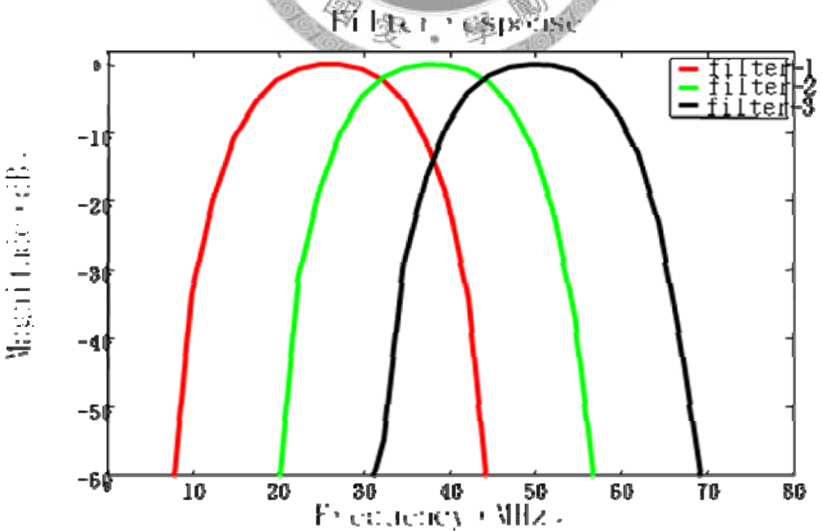

Fig. 7.3 Frequency (magnitude) response of three filters for subband imaging

Simulation methods described in the chapter 4 were adopted. In the simulations, the lateral beam patterns at 10mm, and 10.5mm of SEUT and SEAT were calculated. The signals were then convolved with three Gaussian filters to obtain the subband signals. Experiments under a similar setup were also performed. A 25 μm gold wire was placed at 10mm and 10.5mm from the transducer surface. The three Gaussian filters were also applied. The lateral projection of subband signals of SEUT and SEAT are shown in Fig. 7.4 and 7.5. The subband signals on the focal point (10.5mm) of SEUT and SEAT have the similar performance. It is shown that with SEAT, it is possible to improve lateral resolution when out of the geometric focus. Table 7.1 and 7.2 shows the simulation and experimental results of lateral resolution.

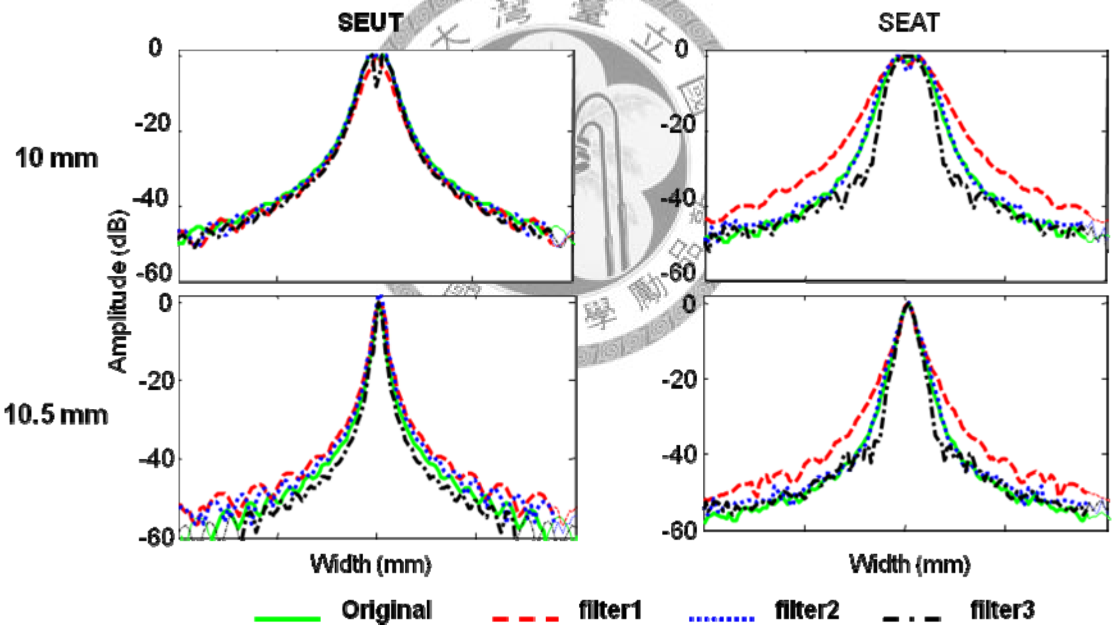

Fig 7.4 Subband beam plots form simulations

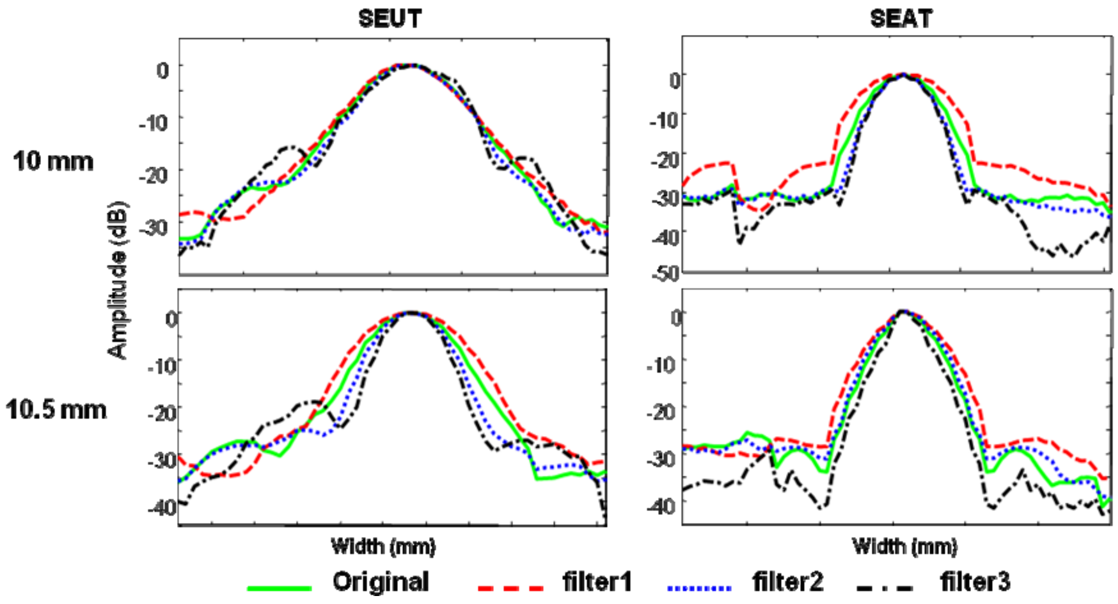

Fig 7.5 Subband beam plots from experiments

Table 7.1 The simulation results of lateral resolution

Depth	SEUT Original	SEUT Subbnad1	SEUT Subbnad2	SEUT Subbnad3	SEAT Original	SEAT Subbnad1	SEAT Subbnad2	SEAT Subbnad3
10.0mm	336	256	337	332	403	496	452	334
10.5mm	91	124	92	76	110	124	103	93

Table 7.2 The experimental results of lateral resolution

Depth	SEUT Original	SEUT Subbnad1	SEUT Subbnad2	SEUT Subbnad3	SEAT Original	SEAT Subbnad1	SEAT Subbnad2	SEAT Subbnad3
10.0mm	138	140	133	141	92	128	81	80
10.5mm	99	120	85	75	95	102	97	71

7.4 Multi-modality imaging

In addition to the possible future works described in this chapter, another possible future work of this research is the integration of all technologies developed in this thesis. In particular, it is of interest to combine ultrasonic imaging with photoacoustic imaging. The SEAT can be used to provide a wide bandwidth for ultrasonic imaging, whereas the DFPT can be applied for *in vivo* investigation with gold nanoparticles to be the photoacoustic molecular probe. This will be beneficial for cancer research on small animal models.

References

[1] S. K. Burley, S. C. Almo, J. B. Bonanno, et al. Structural genomics: Beyond the human genome project. Nature Genet, vol, 23, pp.151–157, 1999.

[2] M. S. Clark, “Comparative genomics: The key to understanding the human genome project”, Bioessays, vol. 21, pp. 121–130. 1999;

[3] R. D. Phair and T. Misteli, “Kinetic modelling approaches to in vivo imaging”, Nat. Rev. Mol. Cell. Biol. Vol. 2, pp. 898–907, 2001.

[4] M. Gassmann and T. Hennet, ”From genetically altered mice to integrative physiology”, News Physiol. Sci,.vol. 13, pp. 53–57, 1998.

[5] R. S. Balaban and V. A. Hampshire, ”Challenges in small animal noninvasive imaging”, ILAR J. vol.42 , pp. 248–262, 2001.

[6] V. Koo, P. W. Hamilton and K. Williamson,”Non-invasive *in vivo* imaging in small animalresearch”, Cellular Oncology vol. 28, 127–139,2006

[7] T. L. Szabo, Diagnostic Ultrasound Imaging: Inside Out. Burlington, MA: Elsevier, 2004

[8] K. K. Shung, "Advances in ultrasound," IEEE Eng. Med. Biol, vol. 15, pp. 18-19, Nov-Dec 1996.

[9] G. R. Lockwood, D. H. Turnbull, D. A. Christopher, and F. S. Foster, "Beyond 30 MHz - Applications of high-frequency ultrasound imaging," IEEE Eng. Med. Biol, vol. 15, pp. 60-71, Nov-Dec 1996.

[10] F. S. Foster, C. J. Pavlin, K. A. Harasiewicz, D. A. Christopher, and D. H. Turnbull, "Advances in ultrasound biomicroscopy," Ultrasound in Medicine and Biology, vol. 26, pp. 1-27, Jan 2000.

[11] S. Yusuf, S. Reddy, S. Ôunpuu and S. Anand, “Global burden of cardiovascular diseases: part I: general considerations, the epidemiologic transition, risk factors, and

impact of urbanization," Circulation, vol. 104, no. 22, pp. 2746–2753, 2001.

[12] G. A. Kaplan, J. E. Keil, "Socioeconomic factors and cardiovascular disease: a review of the literature.," Circulation, vol. 88, pp. 1973-1998, 1993.

[13] C. A. Milano, L.F. Allen, H. A. Rockman, P.C. Dolber, T. R. McMinn and K. R. Chien, et al., "Enhanced myocardial function in transgenic mice overexpressing the beta 2-adrenergic receptor, " Science, vol. 264, no. 5158, pp. 582–586, 1994.

[14] S. Srinivasan, H. S. Baldwin, O. Aristizabal, L. Kwee, M. Labow and M. Artman, et al., "Noninvasive, in utero imaging of mouse embryonic heart development with 40-MHz echocardiography," Circulation, vol. 98, no. 9, pp. 912–918, 1998.

[15] N. Tanaka, N. Dalton, L. Mao, A. H. Rockman, L. K. Peterson and R. K. Gottshall, et al. "Transthoracic echocardiography in models of cardiac disease in the mouse," Circulation, vol. 94, no. 5, pp. 1109–1117, 1996.

[16] M. Scherrer-Crosbie, W. Steudel, R. Ullrich, P. R. Hunziker, N. Liel-Cohen and J. Newell, et al. "Echocardiographic determination of risk area size in a murine model of myocardial ischemia," Am. J. Physiol., vol. 277, no. 3, pp. H986–H992, 1999.

[17] L. Brown, A. Fenning, V. Chan, D. Loch, K Wilson and B. Anderson, et al., "Echocardiographic assessment of cardiac structure and function in rats," Heart Lung Circ., vol. 11, no. 3, pp. 167–173, 2002.

[18] N. Tanaka, N. Dalton, L. Mao, H. A. Rockman, K. L. Peterson, K. R. Gottshall, J. J. Hunter, K. R. Chien, J. Ross, "Transthoracic echocardiography in models of cardiac disease in the mouse", Circulation, vol. 94, pp.1109-1117. 1996

[19] X. P. Yang, Y. H. Liu, N. E. Rhaleb, N. Kurihara, H. E. Kim, O. A. "Carretero, Echocardiographic assessment of cardiac function in conscious and anesthetized mice." Am J Physiol 277(Pt2):H1967-H1974, 1999.

[20] F. S. Foster, C. J. Pavlin, K. A. Harasiewicz, D. A. Christopher, D. H. Turnbull,

"Advances in ultrasound biomicroscopy" Ultrasound Med Biol 26:1-27, 2000

[21] M. C. Gilardi, G. Rizzo, A Savi and F Fazio, "Registration of multi-modal biomedical images of the heart," Q. J. Nucl. Med., vol. 40, no. 1, pp. 142–150, 1996

[22] T. Makela, P. Clarysse, O. Sipila, N. Pauna, Q. C. Pham and T. Katila, et al., "A review of cardiac image registration methods," IEEE Trans. Med. Imaging, vol. 21, no. 9, pp. 1011–1021, 2002.

[23] B. Desjardins and E. A. Kazerooni, "ECG-gated cardiac CT," Am. J. Reontgenol., vol. 182, no. 4, pp. 993–1010, 2004.

[24] M. L. Li, W. J. Guan and P. C. Li, "Improved synthetic aperture focusing technique with application in high frequency ultrasound imaging," IEEE Trans. Ultrason. Ferroelectr. Freq. Control, vol. 51, no. 1, pp. 63–70, 2004.

[25] M. O'Donnell, "Coded excitation system for improving the penetration of real-time phased-array imaging systems," IEEE Trans. Ultrason. Ferroelectr. Freq. Control, vol. 39, no. 3, pp. 341–351, 1992.

[26] J. W. Adams, "A new optimal window," IEEE Trans. Signal Process., vol. 39, no. 8, pp. 1753-1769, 1991.

[27] S. G. Nash and A. Sofer, Linear and Nonlinear Programming. New York: McGraw-Hill, 1996

[28] Cardiac Cycle, http://perfline.com/notebook/cycle.html.

[29] X. H. T. Wehrens, S. Kirchhoff and P. A. Devendans, "Mouse electrocardiography: an interval of thirty years," Cardiocasc. Res., vol.45, pp. 231-237, 2000

[30] G. S. Kino: Acoustic Waves. Prentice-Hall, Englewood Cliffs, NJ, 1987.3.1.1

[31] K. K. Shung, J. M. Cannata, and Q. F. Zhou, "Piezoelectric materials for high frequency medical imaging applications: A review," J. Electroceram, vol. 19, pp. 141–147, 2007.

[32] B. Jaffe, W. R. Cook and H. Jaffe, Piezoelectric ceramics, Academic Press, London, UK, 1971

[33] IEEE standard on piezoelectricity, ANSI/IEEE Std. 176-1987, Jan. 1988

[34] W. A. Smith, in Proc. 1989 IEEE Ultrason. Symp., vol. 1, (1989), p. 755,

[35] Collin R. E., "Theroy and design of wide-band multisection quarter-wave transformers.," Proc. IRE, pp.197-185,1955

[36] C. S. Desilets, J. D. Fraser, G. S. Kino. "The design of efficient broad-band piezoelectric transducers". IEEE Trans. Sonics Ultras. 25: 115, 1978.

[37] L. E. Kinsler, A. R. Frey, A. B. Coppens, J. V. Sanders, "Fundamentals of Acoustics", 3rd Ed. John Wiley, New York, 1982.

[38] A. R. Selfridge,"Approximate material properties in isotropic materials.," IEEE Trans. Son. Ultras.32: 381, 1985.

[39] S. Thiagarajan , I. Jayawyrdena, R. W. Martin," Design of 20 MHz wideband piezoelectric transducers for close-proximity imaging." Biomed. Sei. Instru. 27: 57, 1991.

[40] M. I. Haller, B. T. Khuri-Yakub, "Tapered acoustic matching layers." IEEE Ultrasonics Symp. Proc., 505, 1994.

[41] C. M. Sayers, C. E. Tait, "Ultrasonic properties of transducer backings." Ultrasonics, 22: 57,1984.

[42] M. G. Grewe, " Acoustic properties of particleipolymer composites for ultrasonic transducer backing applications." *IEEE Truns. U1-trus. Ferro.* ***Freq.*** *Cont.* 37: *506,* 1990.

[43] S. Rhee, T. A. Ritter, K. K. Shung, H. Wang, W. Cao, "Materials for acoustic matching in ultrasound transducers" IEEE Ultrasonics Symposium, Vol 2, pp.:1051 – 1055,2001

[44] W. Haifeng, T. A. Ritter, C. Wenwu, K. K. Shung, “High frequency properties of passive materials for ultrasonictransducers,” vol.48, pp. 78-84, 2001

[45] G. R. Lockwood, D. H. Turnbull, and F. S. Foster, "Fabrication of high frequency spherically shaped ceramic transducers," IEEE Trans. Ultrason. Ferroelectr. Freq. Control, vol. 41, pp. 231–235, 1994.

[46] J. M. Cannata, T. A. Ritter, W. H. Chen, R. H. Silverman, and K. K. Shung, "Design of efficient, broadband single-element (20-80 MHz) ultrasonic transducers for medical imaging applications," IEEE Trans. Ultrason. Ferroelectr. Freq. Control, vol. 50, pp. 1548–1557, 2003.

[47] D. H. Turnbull, B. G. Starkoski, K. A. Harasiewicz, J. L. Semple, L. From, A. K. Gupta, D. N. Sauder, and F. S. Foster, "40-100 MHz B-scan ultrasound backscatter microscope for skin imaging," Ultrasound Med. Biol., vol. 21, pp. 79–88, 1995.

[48]D. J. Coleman, R. H. Silverman, A. Chabi, M. J. Rondeau, K. K. Shung, J. Cannata, and H. Lincoff, "High-resolution ultrasonic imaging of the posterior segment," Ophthalmology, vol. 111, pp. 1344–1351, 2004.

[49] F. S. Foster, M. Y. Zhang, A. S. Duckett, V. Cucevic, and C. J. Pavlin, "In vivo imaging of embryonic development in the mouse eye by ultrasound biomicroscopy," Invest. Ophthalmol. Vis. Sci., vol. 44, pp. 2361–2366, 2003.

[50] K. K. Shung and M. Zipparo, "Ultrasonic transducers and arrays," IEEE Eng. Med. Biol., vol. 15, pp. 20–30, 1996.

[51] J. H. Liu, G. S. Jeng, T. K. Wu and P. C. Li, "ECG triggering and gating for ultrasonic small animal imaging," IEEE Trans. Ultrason. Ferroelectr. Freq. Control, vol. 53, pp. 1590–1596, 2006.

[52] M. L. Li, W. J. Guan, and P. C. Li, "Improved synthetic aperture focusing technique with applications in high-frequency imaging," IEEE Trans. Ultrason. Ferroelectr. Freq.

Control, vol. 51, pp. 63–70, 2004.

[53] J. A. Ketterling, S. Ramachandran, and O. Aristizabal, "Operational verification of a 40-MHz annular array transducer," IEEE Trans. Ultrason. Ferroelectr. Freq. Control, vol. 53, pp. 623–630, 2006.

[54] M. Arditi, F. S. Foster, W. B. Taylor, and J. W. Hunt, "Theory and development of focused annular arrays," Ultrason. Imag., vol. 3, pp. 214–215, 1981.

[55] K. A. Snook, C. H. Hu, T. R. Shrout, and K. K. Shung, "High-frequency ultrasound annular-array imaging. Part I: array design and fabrication," IEEE Trans. Ultrason. Ferroelectr. Freq. Control, vol. 53, pp. 300–308, 2006.

[56] E. J. Gottlieb, J. M. Cannata, C. H. Hu, and K. K. Shung, "Development of a high-frequency (> 50 MHz) copolymer annular-array, ultrasound transducer," IEEE Trans. Ultrason. Ferroelectr. Freq. Control, vol. 53, pp. 1037–1045, 2006.

[57] E. W. Cherin, J. K. Poulsen, A. F. W. van der Steen, P. Lum, and F. S. Foster, "Experimental characterization of fundamental and second harmonic beams for a high-frequency ultrasound transducer," Ultrasound Med. Biol., vol. 28, pp. 635–646, 2002.

[58] C. C. Shen and P. C. Li, "Pulse-inversion-based fundamental imaging for contrast detection," IEEE Trans. Ultrason. Ferroelectr. Freq. Control, vol. 50, pp. 1124–1133, 2003.

[59] C. C. Shen, Y. H. Chou, and P. C. Li, "Pulse inversion techniques in ultrasonic nonlinear imaging," J. Med. Ultrasound, vol. 13, pp. 3–17, 2005.

[60] Y. C. Cheng, C. C. Shen, and P. C. Li, " Nonlinear pulse compression in pulse-inversion fundamental imaging," Ultrason Imaging, vol. 29, pp. 73–86, 2007.

[61] K. A. Snook, J. Z. Zhao, C. H. F. Alves, J. M. Cannata, W. H. Chen, J. J. Meyer Jr, T. A. Ritter, and K. K. Shung, "Design, fabrication, and evaluation of high frequency,

single-element transducers incorporating different materials," IEEE Trans. Ultrason. Ferroelectr. Freq. Control, vol. 49, pp. 169–176, 2002.

[62] J. M. Cannata, T. A. Ritter, W. H. Chen, R. H. Silverman, and K. K. Shung, "Design of efficient, broadband single-element (20-80 MHz) ultrasonic transducers for medical imaging applications," IEEE Trans. Ultrason. Ferroelectr. Freq. Control, vol. 50, pp. 1548–1557, 2003.

[63] K. Nakamura, K. Fukazawa, K. Yamada, and S. Saito, "Broadband ultrasonic transducers using a LiNbO3 plate with a ferroelectric inversion layer," IEEE Trans. Ultrason. Ferroelectr. Freq. Control, vol. 50, pp. 1558–1562, 2003.

[64] Q. F. Zhou, J. M. Cannata, H. K. Guo, C. Z. Huang, V. Z. Marmarelis, and K. K. Shung, "Half-thickness inversion layer high-frequency ultrasonic transducers using LiNbO3 single crystal," IEEE Trans. Ultrason. Ferroelectr. Freq. Control, vol. 52, pp. 127–133, 2005.

[65] Q. F. Zhou, J. Cannata, and K. K. Shung, "Design and modeling of inversion layer ultrasonic transducers using LiNbO3 single crystal," Ultrasonics, vol. 44, pp. e607–e611, 2006.

[66] K. Nakamura, K. Fukazawa, K. Yamada, and S. Saito, "An ultrasonic transducer for second harmonic imaging using a LiNbO3 plate with a local ferroelectric inversion layer," IEEE Trans. Ultrason. Ferroelectr. Freq. Control, vol. 53, pp. 651–655, 2006.

[67] R. E. McKeighen, "Design guidelines for medical ultrasonic arrays," Proc. SPIE, vol. 3341, pp. 2–18, 1998.

[68] Q. F. Zhou, J. Cannata and K. K. Shung, “Design and modeling of inversion layer ultrasonic transducers using LiNbO3 single crystal, Ultrasonics, Vol. 44, pp. e607-e611, 2006.

[69] J. Kushibiki, I. Takanaga, M. Arakawa, T. Sannomiya, Accurate measurements of

the acoustical physical constants of LiNbO3 and LiTaO3 single crystals, IEEE Trans. Ultrason. Ferroelectr. Freq. Control 46 (1999) 1315–1323

[70] J. M. Cannata, T. A. Ritter, W. H. Chen, R. H. Silverman, and K. K. Shung, "Design of efficient, broadband single-element (20-80 MHz) ultrasonic transducers for medical imaging applications," IEEE Trans. Ultrason. Ferroelectr. Freq. Control, vol. 50, pp. 1548–1557, 2003.

[71] Q. F. Zhou, J. M. Cannata, H. K. Guo, C. Z. Huang, V. Z. Marmarelis, and K. K. Shung, "Half-thickness inversion layer high-frequency ultrasonic transducers using LiNbO3 single crystal," IEEE Trans. Ultrason. Ferroelectr. Freq. Control, vol. 52, pp. 127–133, 2005.

[72] H. F. Zhang, K. Maslov, G. Stoica, and L.-H. Wang, "Functional photoacoustic microscopy for high-resolution and noninvasive in vivo imaging," *Nature Biotechnology*, vol 24, pp.848–851, 2006

[73] W. F. Cheong, S. A. Prahl, and A. J. Welch, "A Review of the Optical-Properties of Biological Tissues," *IEEE J. Quantum Electron.*, vol. 26, pp. 2166-2185, 1990.

[74] M. Hejazi, M. Abolhassani, A. Ahmadian, M. Frenz, M. Jaeger, J. Niederhauser, A. Amjadi, "A Comparison of Laser-Ultrasound Detection System Sensitivity with a Broad-Band Ultrasonic Source for Biomedical Applications," *Archives of Medical Research,* Vol 37, pp. 322 – 327, 2005

[75] K. P. Köstli, M. Frenz, P. Weber, G. Paltauf, and H. Schmidt-Kloiber, ''Optoacoustic tomography: time-gated measurement of pressure distributions and image reconstruction,'' *Appl. Opt.*, Vol.40, 3800–3809, 2001.

[76] J. J. Niederhauser, D. Frauchiger, H. P. Weber, and M. Frenz, ''Realtime optoacoustic imaging using a Schlieren transducer,'' *Appl. Phys. Lett.*, vol 81, 571–573, 2002.

[77] A. A. Karabutov, E. V. Savateeva, N. B. Podymova, A. A. Oraevsky, "Backward mode detection of laser-induced wide-band ultrasonic transients with optoacoustic transducer," *J. Appl. Phys.,* vol.87 pp. 2003-2014, 2000.

[78] J. T. Oh, M. L. Li, L. V.Wang, and K. Maslov"Three-dimensional imaging of skin melanoma in vivo by dual-wavelength photoacoustic microscopy", *J. Biomed. Opt.*, vol.11, pp.0340321-4, 2006.

[79] R. G. M. Kolkman, E. Hondebrink, W. Steenbergen, and F. F. M. de-Mul, "In vivo photoacoustic imaging of blood vessels using an extreme-narrow aperture sensor," *IEEE J. Select. Topics. Quantum Electron.,* vol. 9, pp. 343-346, 2003.

[81] V. Tuchin, Tissue Optics. Light Scattering Methods and Instruments for Medical Diagnosis, SPIE Press, Bellingham, WA , 2000.

[82] C. W. Wei, Y. L. Sheu and P. C. Li, "Photoacoustic contrast enhancement using selective subband imaging: experimental results", *SPIE International Symposium on Biomedical,* 2007.

[83] Y. L. Sheu, C. W. Wei and P. C. Li, "Effects of absorption properties on photoacoustic spectral characteristics: numerical analysis", S*PIE International Symposium on Biomedical Optics,* 2007.

[84] K. A. Snook, J. Z. Zhao, C. H. F. Alves, J. M. Cannata, W. H. Chen, J. J. Meyer Jr, T. A. Ritter, and K. K. Shung, "Design, fabrication, and evaluation of high frequency, single-element transducers incorporating different materials," *IEEE Trans. Ultrason.* Ferroelectr. Freq. Control, vol. 49, pp. 169–176, 2002.

[85] V. E. , Gusev and A. A. Karabutov, *Laser Optoacoustics*, Chap 2, pp45~48. *American Institute of Physics,* New York, 1993

[86] D. H. Huang, C. K. Liao, C. W. Wei, and Pai-Chi Li, "Simulations of optoacoustic wave propagation in light-absorbing media using a finite-difference time-domain

method," *J. Acoust. Soc. Am,* 117 (5), May 2005.

[87] J. M. Cannata, J. A. Williams, Q. Zhou, T. A. Ritter, and K. K. Shung, “Development of a 35-MHz piezo-composite ultrasound array for medical imaging,” *IEEE Trans. Ultrason., Ferroelect., Freq. Contr.*, vol. 53, pp. 224–236, 2006

[88] M. Lukacs, J. Yin, G. Pang, R. C. Garcia, E. Cherin, R. Williams, J. Mehi, and F. S. Foster, “Performance and characterization of new micromachined high-frequency linear arrays,” *IEEE Trans. Ultrason., Ferroelect., Freq. Contr.*, vol. 53, pp. 1719–1729, 2006.

[89] J. A. Brown, F. S. Foster, and G. R. Lockwood, “A 40 MHz linear array based on a 1-3 composite with geometric elevation focusing,” in *Proc. IEEE Ultrason. Symp.*, 2006, pp. 256–259.

[90] L. Sun, W. D. Richard, J. M. Cannata, C. C. Feng, J. A. Johnson, J. T. Yen, and K. K. Shung,” A high-frame rate high-frequency ultrasonic system for cardiac imaging in mice.” *IEEE Trans. Ultrason., Ferroelect., Freq. Contr.*,Vol.54, pp.1648-55, 2007

[91] J. Chen, X. Cheng, I. M. Shen, J. H. Liu, P. C. Li and M. Wang, "A Monolithic Three-Dimensional Ultrasonic Transducer Array for Medical Imaging", Journal of Microelectromechanical Systems, Vol. 16, No. 5, pp. 1015-1024, October, 2007.

[92]. J. Chen, X. Cheng, C. Chen, P. C. Li, J. Liu, and Y. Cheng, "A Capacitive Micromachined Ultrasonic Transducer Array for Minimally Invasive Medical Diagnosis ", IEEE Journal of MEMS, Vol. 17, no. 3, pp. 599-610, June, 2008.